NASA CR-134845

EXPERIMENTAL INVESTIGATIONS OF ARGON AND XENON ION SOURCES

PREPARED FOR

LEWIS RESEARCH CENTER

NATIONAL AERONAUTICS AND SPACE ADMINISTRATION

GRANT NSG 3011

Annual Report

June 1975

Harold R. Kaufman
Department of Mechanical Engineering
Colorado State University
Fort Collins, Colorado

1. Report No.	2. Government Accession No.	3. Recipient's Catalog No.
NASA CR-134845		

4. Title and Subtitle	5. Report Date
Experimental Investigations of Argon and Xenon Ion Sources	June 1975
	6. Performing Organization Code

7. Author(s)	8. Performing Organization Report No.
Harold R. Kaufman	
	10. Work Unit No.

9. Performing Organization Name and Address	11. Contract or Grant No.
Department of Mechanical Engineering Colorado State University Fort Collins, Colorado 80523	NSG 3011
	13. Type of Report and Period Covered 1 July 1974 - 30 June 1975

12. Sponsoring Agency Name and Address	14. Sponsoring Agency Code
National Aeronautics and Space Administration Washington, D. C. 20546	

15. Supplementary Notes

Grant Manager, Michael J. Mirtich, Jr.
Spacecraft Technology Division
NASA Lewis Research Center
Cleveland, Ohio 44135

16. Abstract

Inert gases are of interest as possible alternatives to the usual electric thruster propellants of mercury and cesium. Xenon is the best inert-gas alternative for conventional missions due to its ease of storage, ease of ionization, and high atomic weight. Argon is a possible alternative if tons of propellant are required (so that cryogenic storage is possible) and excess electric power makes efficiency, and hence atomic weight, less important. Argon is also the preferred propellant in ground applications of thruster technology such as cleaning, micromachining, and ion etching of solid-state devices.

A multipole approach that makes extensive use of flat or cylindrical sheet-metal parts was selected. Minimum discharge losses were in the 200-250 ev/ion range for both argon and xenon. Flatness parameters were typically in the 0.70-0.75 range, which approaches the best values obtained previously in highly optimized designs. When the multipole approach used is properly exploited, it should be possible to rapidly translate initial performance specifications into easily fabricated, high performance prototypes.

17. Key Words (Suggested by Author(s))	18. Distribution Statement
Electrostatic thruster Ion source	Unclassified - Unlimited

19. Security Classif. (of this report)	20. Security Classif. (of this page)	21. No. of Pages	22. Price*
Unclassified	Unclassified	78	$3.00

* For sale by the National Technical Information Service, Springfield, Virginia 22151

NASA-C-168 (Rev. 6-71)

INTRODUCTION

The development of electron-bombardment ion thrusters has been pursued primarily with mercury and cesium propellants. These propellants were chosen for ease of storage, ease of ionization, and high atomic weight. Researchers have demonstrated, however, that electron-bombardment thrusters can be operated on a variety of gases.[1-5] Of the gases considered in these studies, the one best suited to most space propulsion missions is xenon. The high atomic weight and ease of storage (low tankage fraction) are the major factors in this choice. Argon is a possible alternate for space propulsion if tons of propellant are required (so that cryogenic storage is practical) and excess electric power makes efficiency (and hence atomic weight) less important. Argon is also the preferred propellant in ground applications of thruster technology such as cleaning, micromachining, and ion etching of solid-state devices.

A multipole thruster was used to investigate the use of argon and xenon propellants. This thruster is conceptually related to both the multipole design of Moore[6] and Ramsey[7] and the cusped field design of Beattie.[8] The detailed design is similar to the cusped field thruster in that thin pole pieces of soft iron are used with electromagnets between adjacent pole pieces. The major difference from the cusped field thruster is that more and smaller pole peices are used, giving a larger fraction of low-field-strength volume in the ion chamber. The major similarities to the Moore and Ramsey design are the large number of pole pieces used and the general ion-chamber shape. Moore and Ramsey, however, used permanent magnets as pole pieces, with the magnetization

direction towards or away from the center of the ion chamber. If permanent magnets were used in the design studies herein, they would replace the electromagnets between adjacent pole pieces rather than become the pole pieces. As an additional difference, Moore and Ramsey used much higher magnetic field strengths.

The multipole approach was used because of the general high performance level of this type. Although documented performance did not include beam profiles, past experience with a wide range of designs indicated the multipole approach should produce very uniform beams. The specific design employed, using flat and cylindrical rolled sections of sheet metal, was selected for ease of design, fabrication, assembly and modification.

SI (rationalized mks) units are used throughout this paper.

APPARATUS AND PROCEDURE

All testing was conducted in the 1.2-m diameter, 4.6-m long vacuum facility at the Engineering Research Center of the Colorado State University. The pumping was accomplished by an 0.8-m diffusion pump together with liquid-nitrogen cooled liner.

The 15-cm multipole thruster used in this investigation is indicated in Figure 1. The pole pieces are fabricated of 1.5-mm thick soft iron and are 2.5 cm wide. For the wide walls they are flat with an internal diameter of 15 cm, while the upstream pole pieces are cylindrical with mean diameters of 5, 10, and 15 cm. A spacing of 2.5 cm was used for all adjacent pole pieces with 1.5-mm thick aluminum anodes located midway between each pair of pole pieces. Most operation was with anodes flush with pole pieces on the inside of the ion chamber, though some data were obtained with anodes that projected 3 mm beyond the pole pieces. The length of the ion chamber could be varied in 2.5 cm steps by adding or removing anodes and pole pieces.

The original magnetic configuration used 4 electromagnets between each adjacent pair of pole pieces, each electromagnet winding consisting of 21 turns of wire with polymide (Kapton) insulation over a 6-mm diameter core of soft iron. A modified magnetic field configuration was also used with 8 electromagnets between each pair of pole pieces. All electromagnets in each configuration were connected in series, so that the current was the same through all windings. An iron filing map of the magnetic field is shown in Figure 2. The maps for different current levels or different numbers of electromagnets were all similar.

Dished grids were used with a 67 percent open screen and a 43

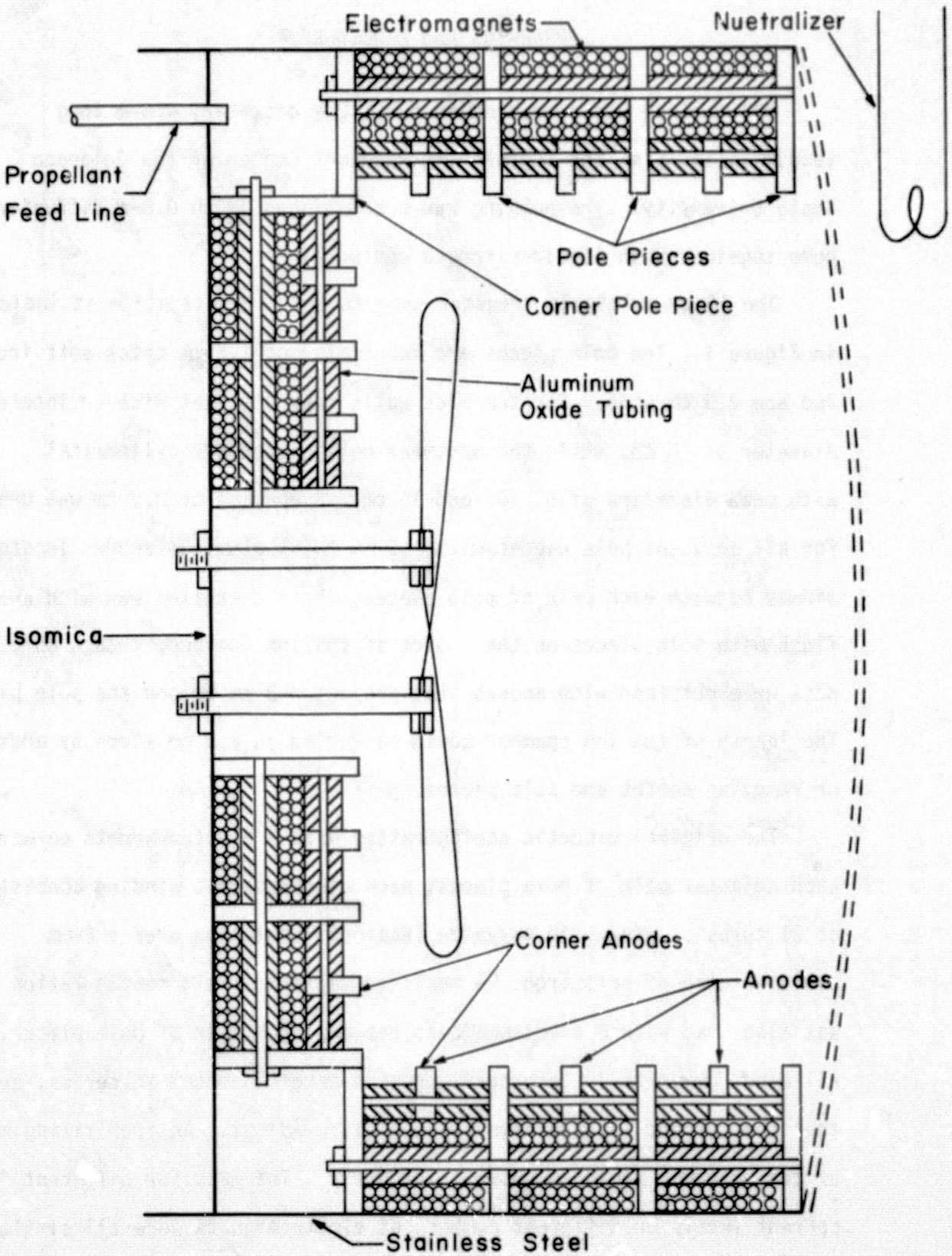

Figure 1. Sketch of 15-cm Multipole Gas Thruster. (7.6 cm Chamber Length Shown.)

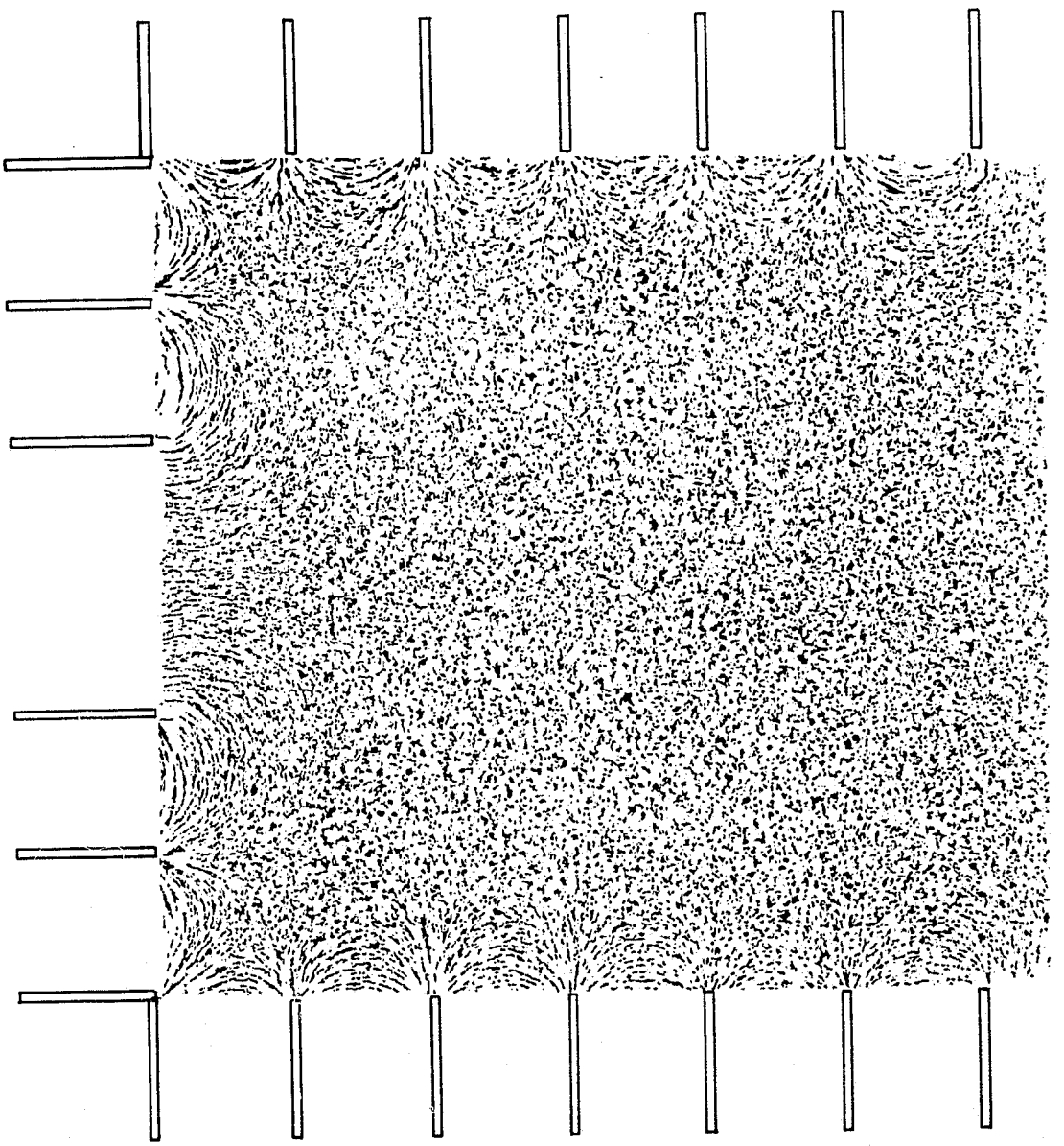

Figure 2. Iron filing magnetic-field map.

percent open accelerator. The thickness of both grids was about 0.4 mm, while the center-to-center hole spacing within a grid was about 2.2 mm. The grids were assembled with a interelectrode gap of about 1 mm and operated with +1000 and -500 volts.

Tungsten wire, 0.25 mm diameter, was used for both main and neutralizer cathodes. The outer shell of the thruster was a tube, rolled from thin stainless steel. The backplate was Isomica. The propellant was introduced into the annular region formed by the two corner pole pieces, with several 6 mm holes through the pole pieces permitting flow radially inwards into the ion chamber.

Electrical power is supplied to the thruster in the manner indicated by Figure 3. Discharge current, discharge voltage, and beam current are displayed on digital voltmeters, as is also indicated in Figure 3. Propellant flow rate was controlled with an adjustable leak valve measured with a mass flowmeter, and maintained within ±1 percent of the desired value while data was being taken.

A Faraday cup probe was installed 6 mm downstream of the center of the accelerator grid, which was installed convex side out. This probe was translated across the beam for current density profiles. A Langmuir probe, moveable in 2 directions was used to obtain plasma data within the ion chamber. Details of both the Faraday and Langmuir probe systems that were used are given by Wilbur.[9] The Langmuir probe data were analyzed using the numerical procedure of Beattie.[10]

Near the end of the investigation an ExB momentum analyzer was installed with the sensing probe 60 cm downstream of the accelerator grid. This instrumentation permitted measurement of the different charge-to-mass ratios in the ion beam. The probe was moveable transverse

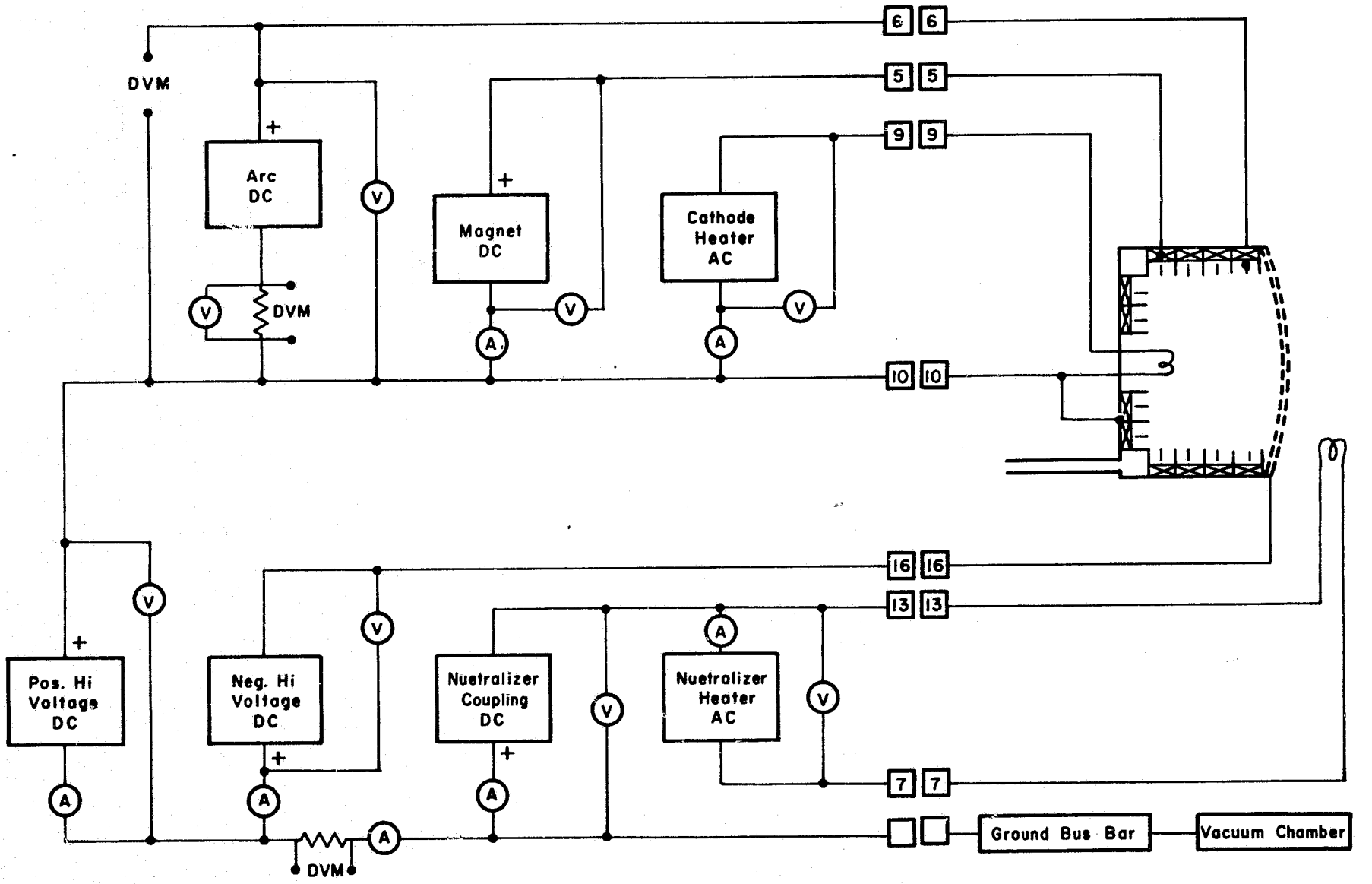

Figure 3. Schematic diagram of power supplies and wiring.

to the ion beam, with the path of motion passing through the center of the ion beam. The probe could also be rotated to maximize the transmitted ion current. The momentum analyzer system is indicated in Figure 4, with details of the sensing probe and its operation being given by Vahrenkamp.[11]

All propellant utilizations presented in this paper were corrected for double ionization and propellant backflow from the vacuum facility. The propellant backflow was calculated from facility pressure and the free-molecular-flow conductance of the accelator system. This correction was small and could have been neglected. The double ionization correction was much larger and the procedure used for this correction is described in the Double Ionization section.

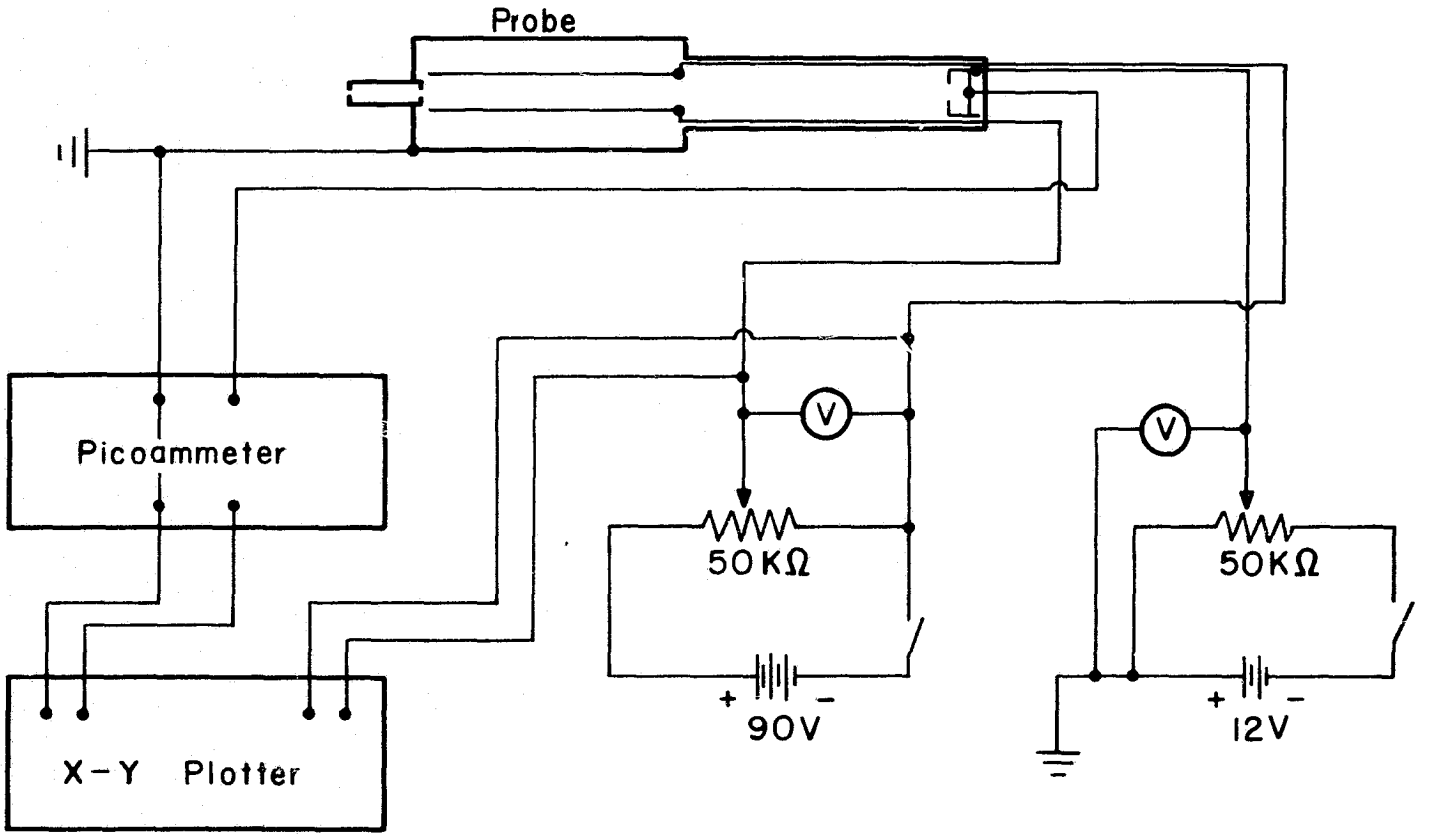

Figure 4. Schematic diagram of ExB momentum analyzer.

MAGNETIC FIELD

Early tests with the anodes that projected 3 mm beyond the pole pieces resulted in excessive discharge losses. A change to the flush anodes gave some improvement. This result suggested that the magnetic field strength was inadequate because the change to flush anodes required electrons to cross more field lines to reach the anodes. This indication of low magnetic field, however, was somewhat ambiguous. As will be shown the discharge loss of the original magnet configuration appeared to approach a minimum at high magnet currents.

The effect of changing the number of electromagnets is indicated in Figure 5 for argon propellant. The discharge loss decreased with increasing magnet current for the 4-magnet configuration, appearing to be near a minimum at 10 amperes. When changed to the eight magnet configuration, though, substantially lower discharge losses were obtained. To explain this apparent discrepancy, detailed magnetic-field measurements were made. The maximum magnetic field is defined as being midway (both radially and axially) between adjacent pole pieces. For a typical maximum value of magnetic field, a side location (not at either end of the chamber) was used. The variation of this typical maximum magnetic field with magnet current is shown in Figure 6 for the two magnet configurations. Figure 6 was then used to plot the discharge data of Figure 5 as a function of maximum magnetic field, which is shown in Figure 7.

It is evident from Figure 7 that the leveling out of discharge losses with magnet current for the 4-magnet configuration (Figure 5) was due, not to the approach of an optimum magnetic field, but to

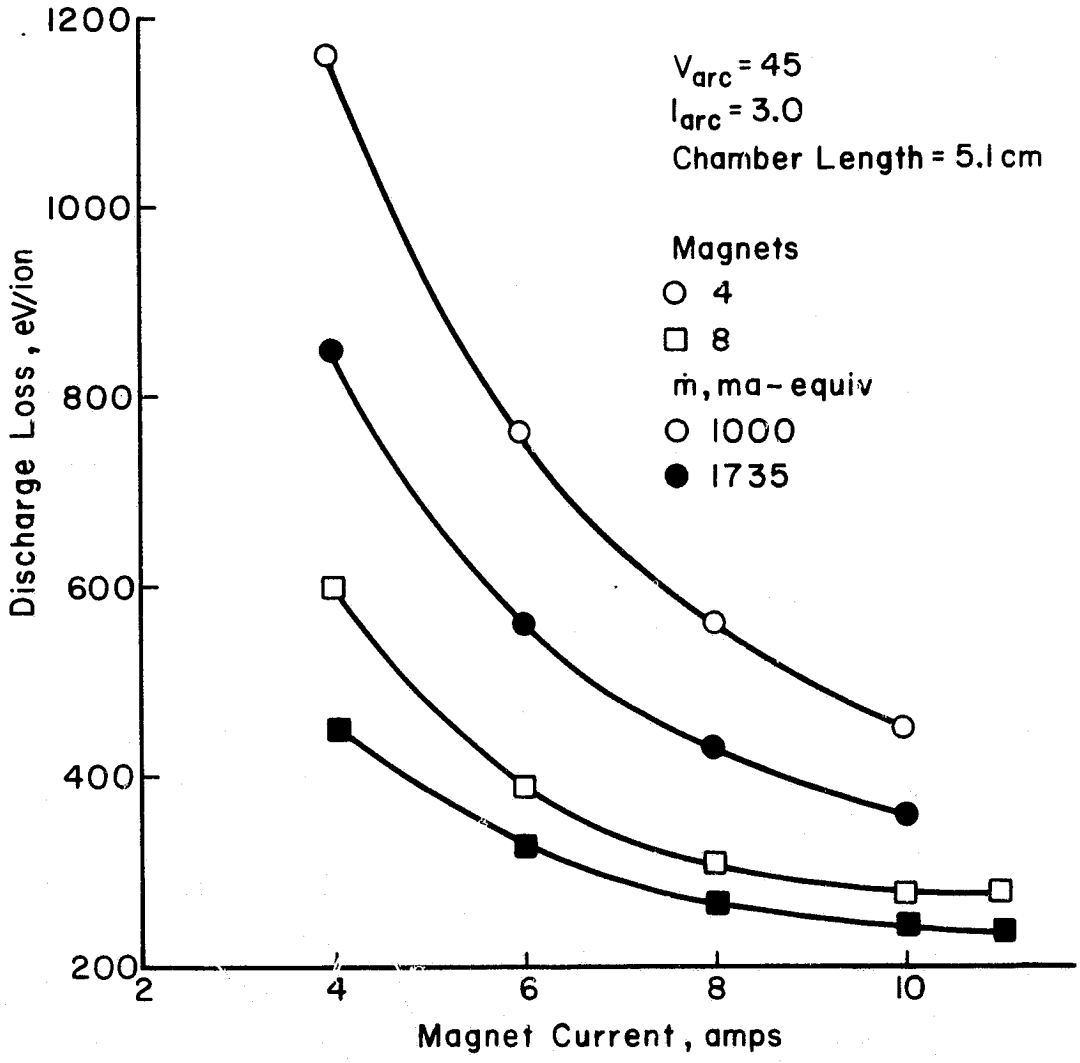

Figure 5. VARIATION OF DISCHARGE LOSS WITH MAGNET CURRENT.

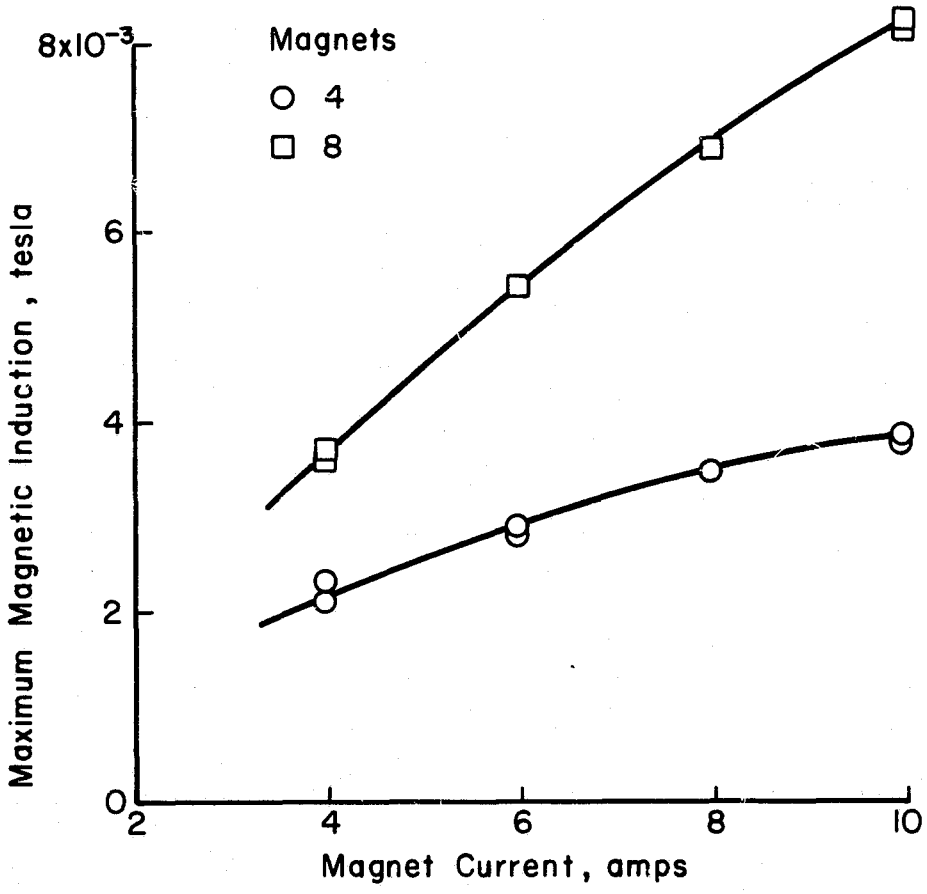

Figure 6. VARIATION OF MAGNETIC FIELD WITH MAGNET CURRENT.

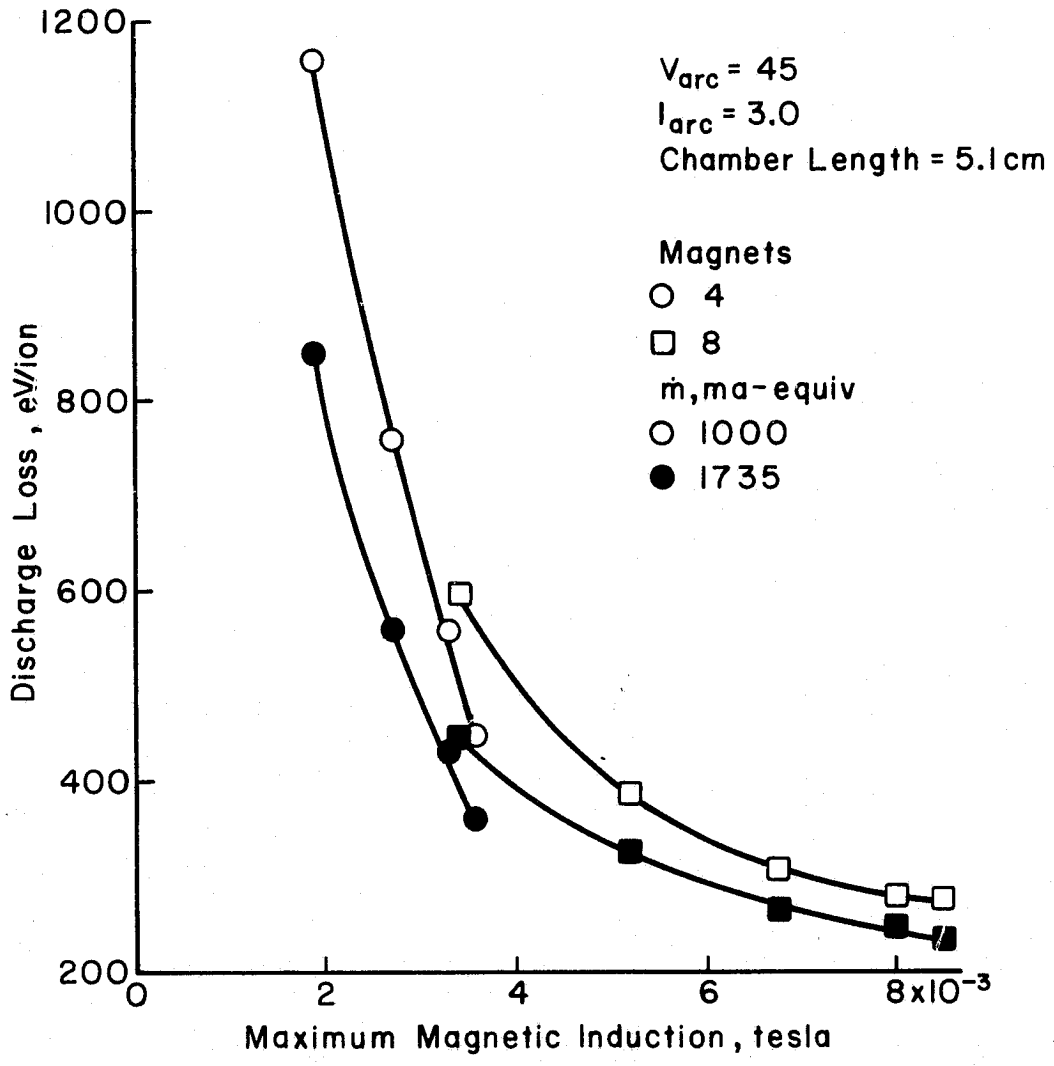

Figure 7. VARIATION OF DISCHARGE LOSS WITH MAGNETIC FIELD.

the approach of saturation in some part of the magnetic circuit. This saturation is evident in the leveling of the 4-magnet magnetic induction between 8 and 10 amperes in Figure 6. As for the optimum strength Figure 7 indicates a maximum magnetic induction near 80×10^{-4} Tesla (80 Gauss) for the 45 volt discharge used. The 4-magnet and 8-magnet data do not quite meet in Figure 7, probably because doubling the number of magnets did not change the field by the same ratio in all parts of the chamber.

The significance of the optimum field strength can be shown with the aid of Figure 8. The primary electrons should be contained within the ion chamber so that they expend most of their energy in producing ions before escaping to the anodes. The fringe magnetic field between adjacent pole pieces should therefore be sufficient that a primary electron cannot, without an intermediate collision, reach an anode. For simplicity, the fringe field is shown in Figure 8(a) as a region of uniform field strength. Picking the direction of motion for a primary electron such that it has the deepest penetration into this fringe field, it is evident from Figure 8(a) that this penetration corresponds to two electron cyclotron radii. The electron cyclotron radius is defined as

$$r_c = 3.37 \times 10^{-6} \sqrt{eV}/B$$

This equation may be rewritten as

$$2r_c B = 6.74 \times 10^{-6} \sqrt{eV}$$

where $2r_c$ is the depth of the fringe field (above the anode) and B is the magnetic induction of this field. The product of $2r_c B$ can therefore be thought of as the flux lines per unit anode length. The distribution of these flux lines normal to the anode is not important. For example, half the magnetic induction extending twice as far from the anode would have

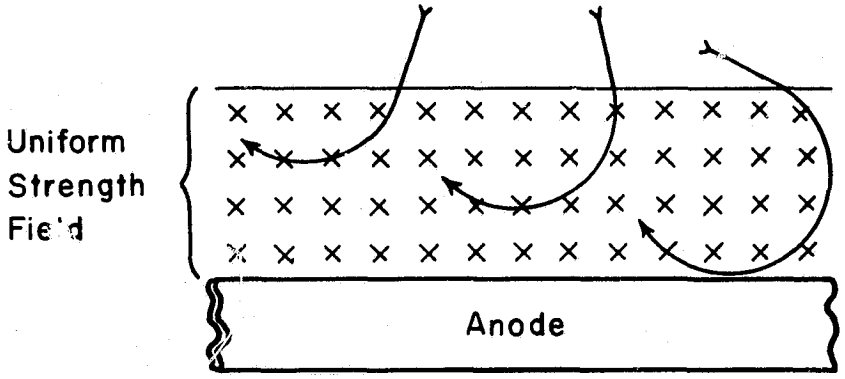

(a) Simplified Deflection Configuration

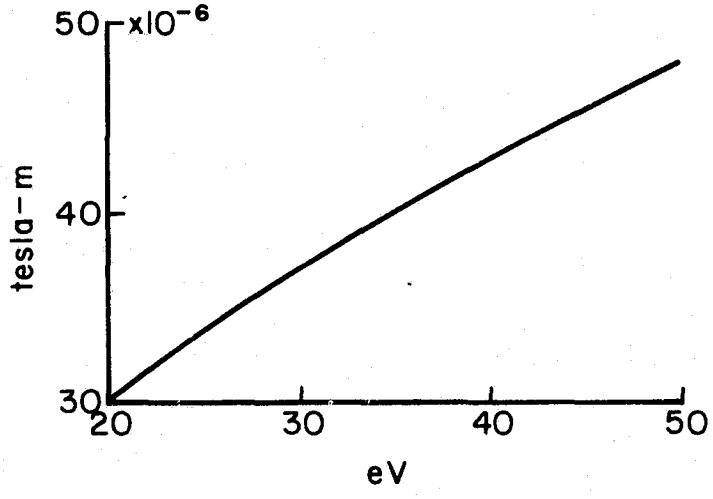

(b) Required Flux per Unit Anode Length as a Function of Electron Energy

Figure 8. Electron interaction with fringe magnetic field above anode.

the same effectiveness in deflecting primary electrons. This conclusion is also valid for the more realistic case of field strength varying with distance from the anode, which can be shown for increments of deflection angle for primary electrons instead of circular orbits. The required flux per unit anode length, from the preceding equation, is shown in Figure 8(b). For comparison of units 50×10^{-6} Telsa-m equals 50 Gauss-cm.

The experimental variation of magnetic induction in the plane of the anode is shown in Figure 9 for a typical side pole-piece location and magnet current of 10 amperes. This side location is typical of most of the ion chamber, and the maximum for this location is the maximum magnetic induction used in Figures 6 and 7. Integration of magnetic induction over distance normal to the anode,

$$\int_{\text{anode}}^{\infty} \overline{B} \times d\overline{\ell},$$

yields the flux per unit anode length. The upper limit of ∞ would apply to a pair of isolated pole pieces. In an ion chamber, the integration is carried to the first point of negligible magnetic field. For the side pole-piece location, numerical integration yielded about 88×10^{-6} Tesla-meters. From Figure 8(b), 45×10^{-6} Tesla-meters should have been sufficient to prevent primary electrons from reaching the anode. An examination of fringe fields at different anode locations showed the weakest field was in the corner location. The corner field, also shown in Figure 9, integrated to 42×10^{-6} Tesla-meters at this same 10 ampere condition. Comparison of these two integrated values with the theoretical value from Figure 8(b) suggests that the escape of primary electrons is controlled by the corner fringe field. This conclusion is supported

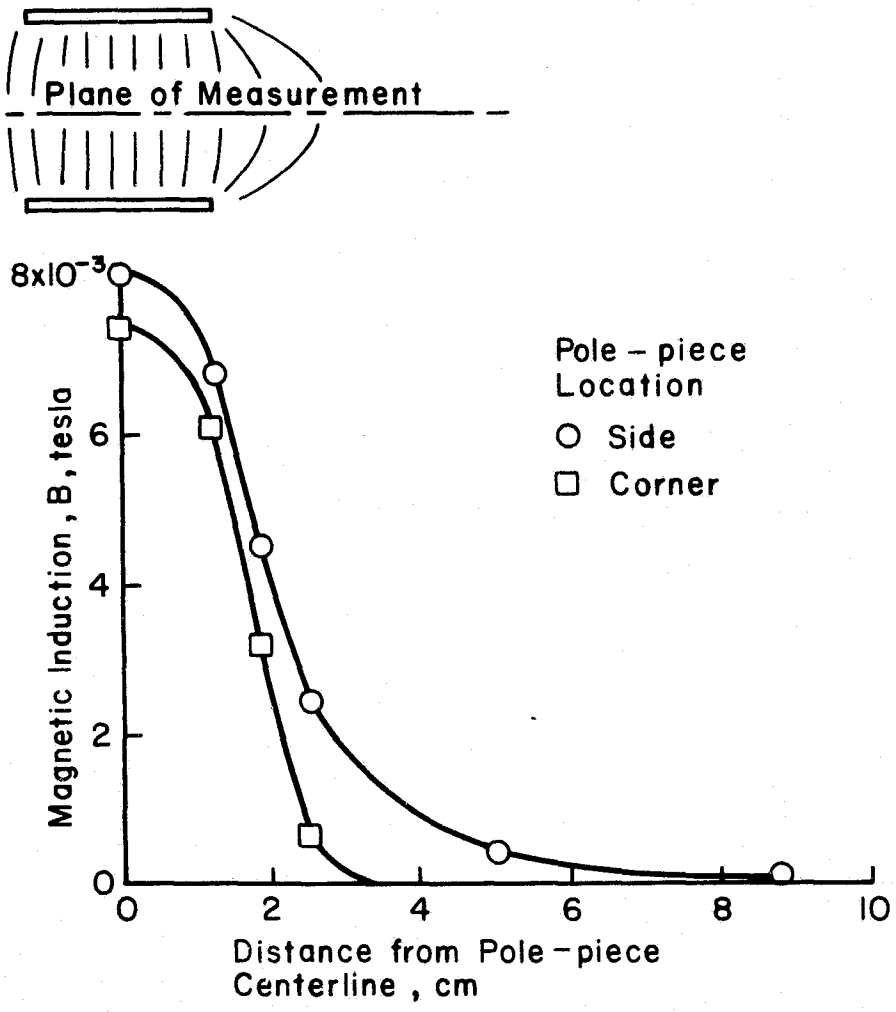

Figure 9. MAGNETIC FIELD BETWEEN POLE PIECES.

by the experimental observation that the corner aluminum anode was more likely to warp during operation.

Some data that can be used for preliminary magnetic-circuit design are shown in Figure 10. Both the actual and ideal magnetic inductions, B_{act} and B_{id}, are based on the minimum cross section of the permeable path. B_{act} uses the measured total flux, while B_{id} uses a calculated flux with the air gap as the only reluctance in the magnetic circuit. The 2:1 spread (from 0.4 to 0.8 of theoretical) is a typical spread for magnetic circuit designs. Because of this spread, it is usually desirable to design with cut-and-try experimental testing, or to over-design by a factor of 2 with derating determined by later experiment. The 4-magnet configuration in Figure 10 is probably lower because the permeable path is nearer constant in cross section for this configuration, hence saturation is approached more simultaneously over a larger volume of permeable material.

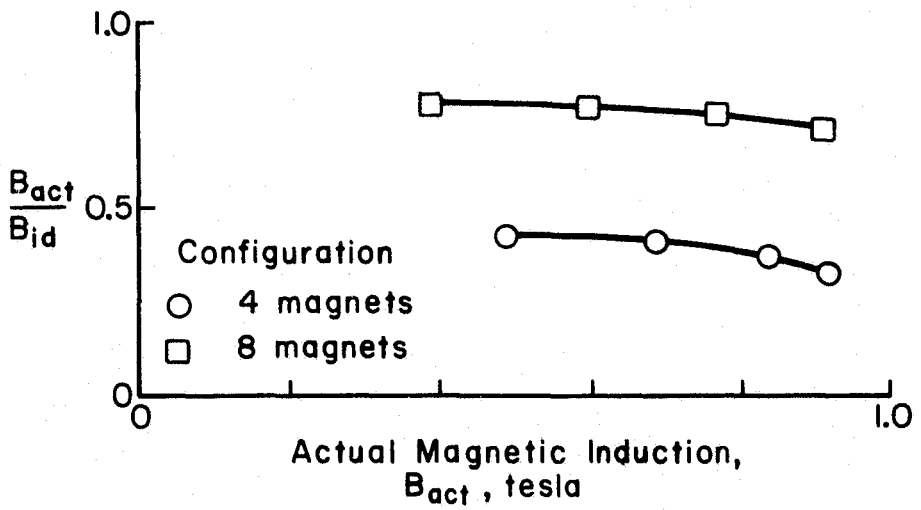

Figure 10. COMPARISON OF ACTUAL AND IDEAL MAGNETIC INDUCTIONS.

ANODE CONFIGURATION

Both Moore[6] and Ramsey[7] indicate that the multipole configuration gave reduced ion losses to ion chamber walls. Experiments conducted by Moore suggested that these ion losses were minimal. On the other hand, ion discharge losses should have been even lower if the majority of the ions produced went into the ion beam. Anode configuration tests were conducted with a 7.6-cm long chamber using both argon and xenon propellants to obtain a preliminary evaluation of this ion-loss problem with the design approach used herein.

Three anode configurations were used in these tests. The configurations were:

(1) All anodes at anode potential (all anode or original configuration);

(2) The anodes adjacent to the corner pole pieces at cathode potential, all others at anode potential (corner out configuration);

(3) The anodes adjacent to the corner pole pieces at anode potential, all others at cathode potential (corner only configuration).

With argon as the propellant, operation was not possible for either the corner out or corner only configurations at less than about a 1300 ma equivalent flow rate. Typical ion-chamber performance at a high flow rate is shown in Figure 11. The corner only configuration gave an increase of about 250 ev/ion over the original configuration, while the corner out gave only a small increase.

The variation of discharge losses with magnet current is shown

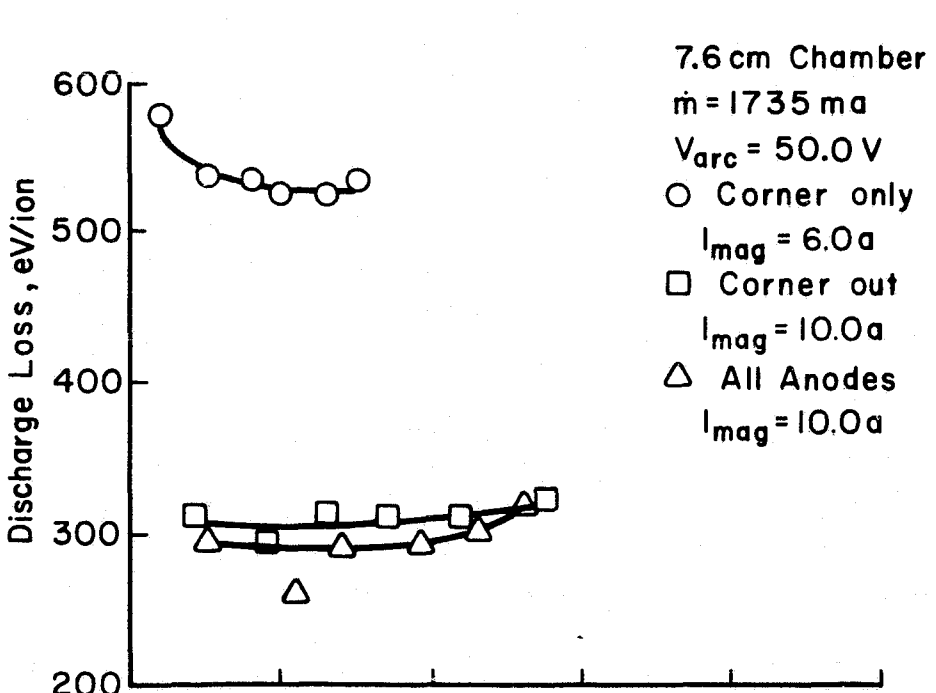

Figure 11. EFFECT OF ANODE CONFIGURATION ON DISCHARGE-CHAMBER PERFORMANCE WITH ARGON PROPELLANT. (ANODE CONFIGURATIONS DEFINED ON PAGE 20.)

in Figure 12 for the same propellant flow rate. As was mentioned in the Magnetic Field section, the thruster has a weaker fringe field above the anodes in the corner than the other anodes. At low magnet currents, where the corner field is not strong enough to prevent electrons from reaching the anodes directly, performance is improved by the exclusion of these corner anodes. At higher magnet currents, where the field strength is sufficient to prevent such direct access by primary electrons, performance is not substantially changed by the exclusion of the corner anodes. The corner only configuration would not operate at magnet currents above 6 amperes, but gave higher discharge losses than either other configuration where operation was possible.

Beam profiles obtained with the three anode configurations are shown in Figure 13. The flatness parameter (average-to-peak current-density ratio) is highest for the original configuration, next highest for the corner out configuration, and lowest for the corner only configuration. The corner only configuration also gave the lowest total beam current, which was the result of constant discharge power and the higher ev/ion with this configuration.

With xenon, operation was possible with all three configurations over the range investigated (220 to 665 ma equivalent). The variation of discharge losses with magnet current is shown in Figures 14 and 15. Except for operation of the corner only configuration at higher magnet currents, the results were similar to those obtained with argon. Xenon beam profiles are shown in Figure 16. These profiles are similar to those obtained with argon, except that the original and corner out profiles are much closer together. This similarity of original and

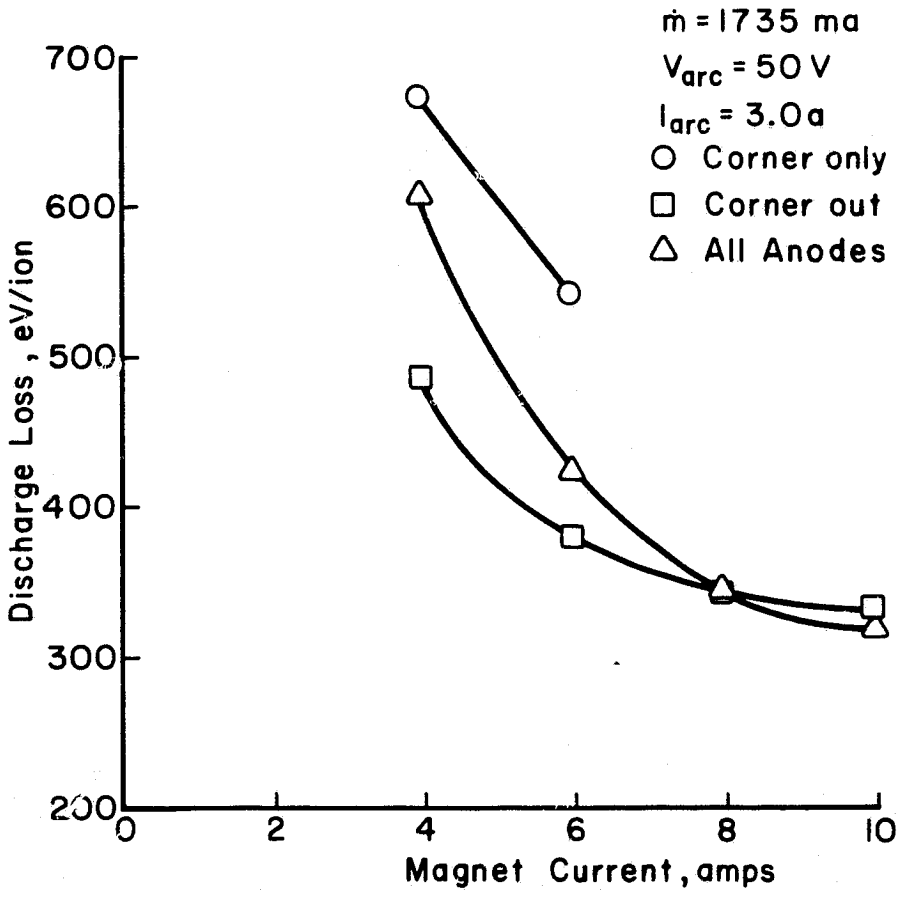

Figure 12. VARIATION OF DISCHARGE LOSS WITH MAGNET CURRENT FOR DIFFERENT ANODE CONFIGURATIONS WITH ARGON PROPELLANT.

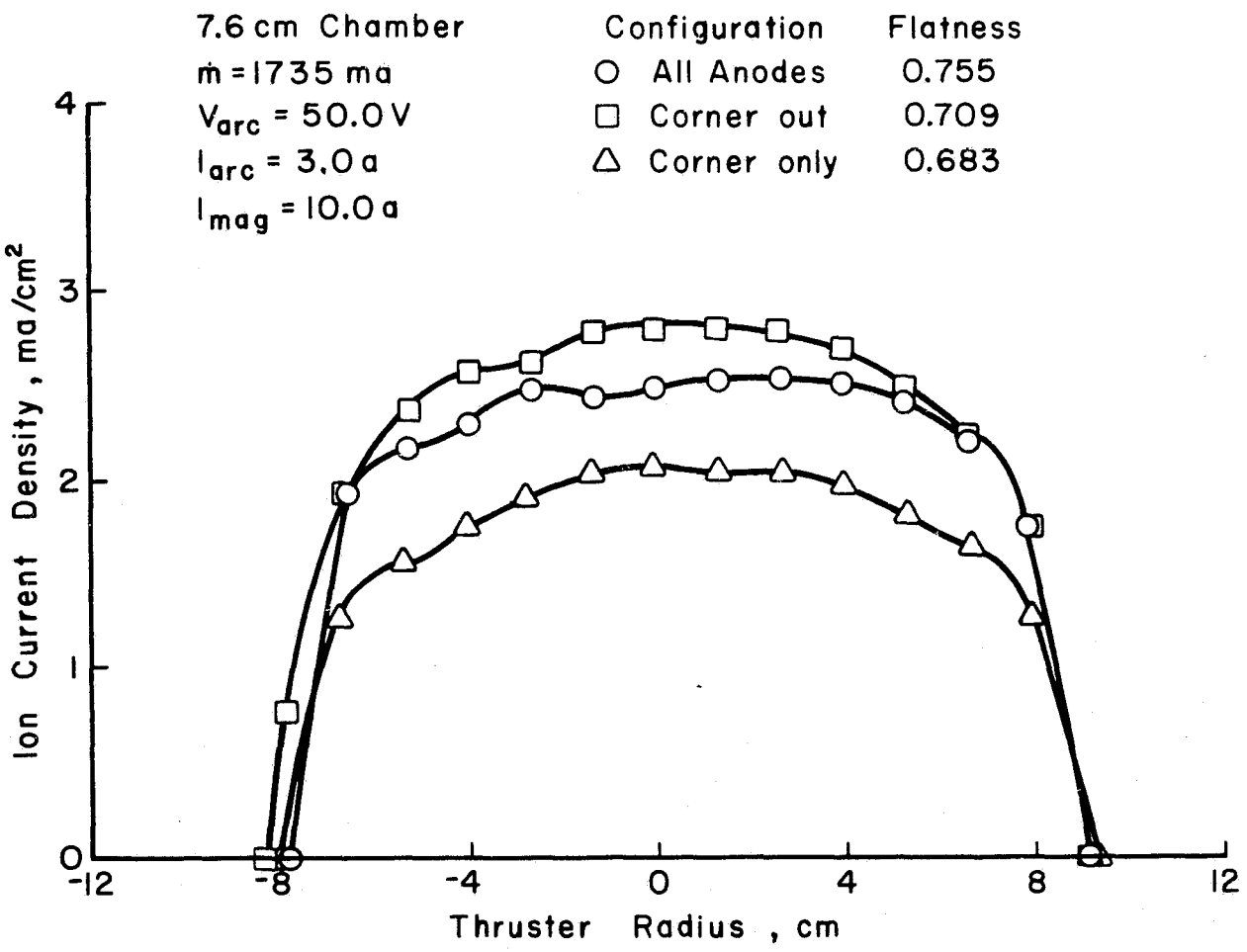

Figure 13. Effect of anode configuration on ion-beam profile with argon propellant.

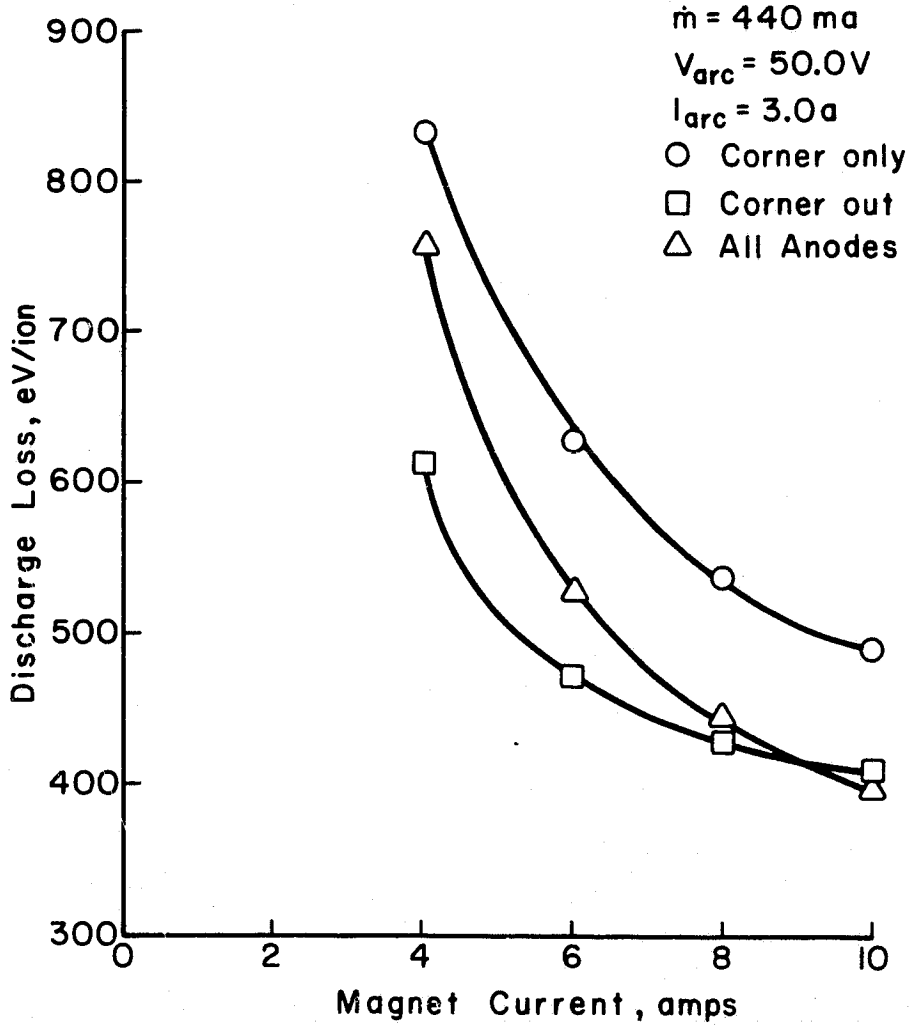

Figure 14. VARIATION OF DISCHARGE LOSSES WITH MAGNET CURRENT FOR DIFFERENT ANODE CONFIGURATIONS WITH XENON PROPELLANT.

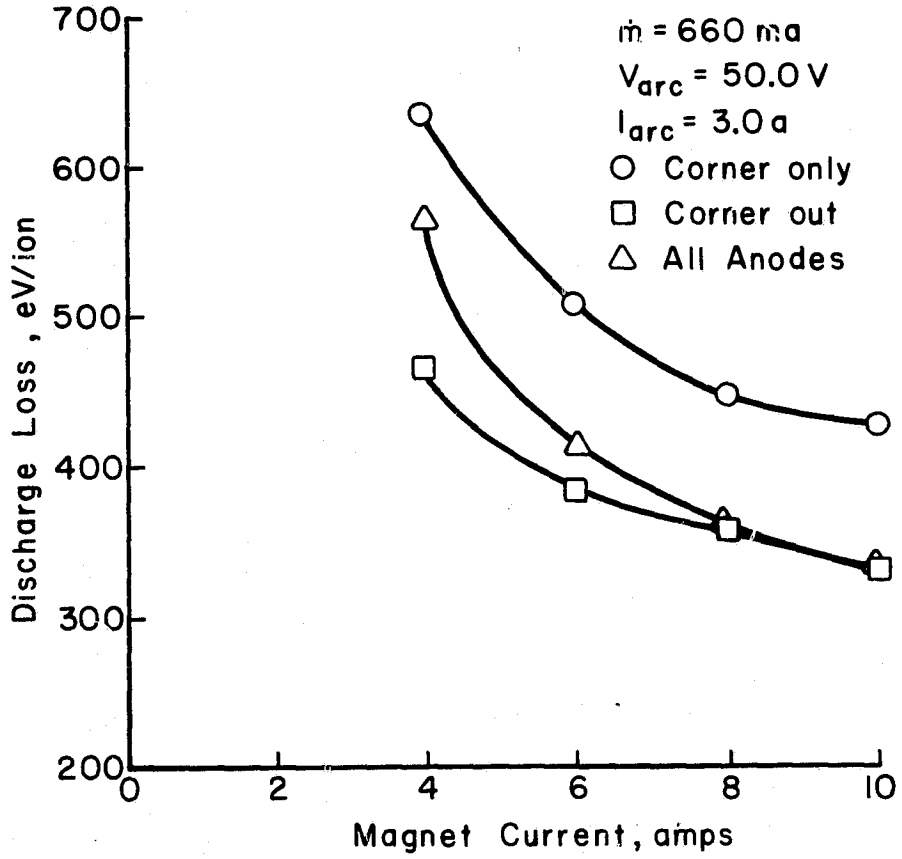

Figure 15. EFFECT OF ANODE CONFIGURATION ON DISCHARGE-CHAMBER PERFORMANCE WITH XENON PROPELLANT.

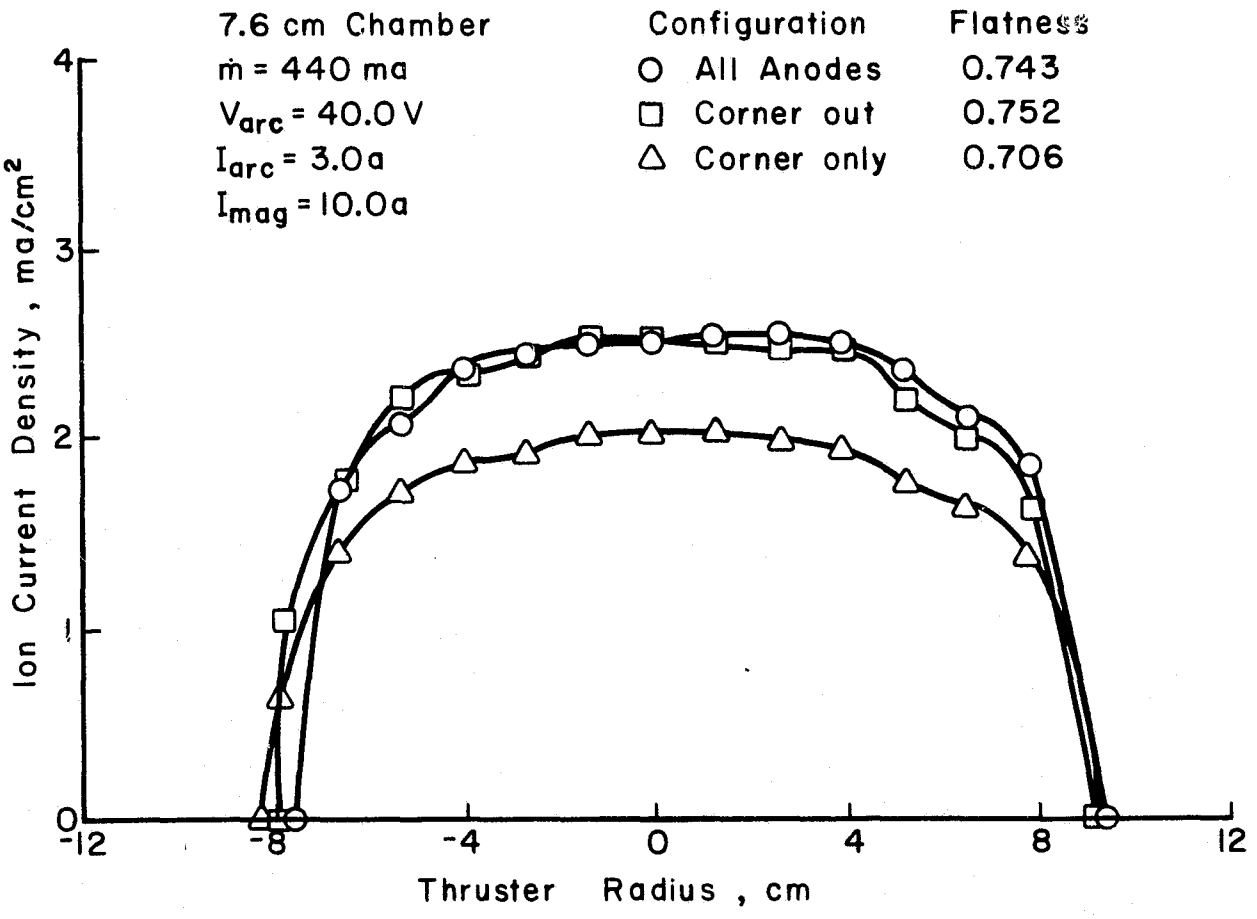

Figure 16. Effect of anode configuration on ion-beam profile with xenon propellant.

and corner out profiles might be due to the higher magnet current used with xenon. As shown in Figure 14 and 15, discharge losses are close at higher magnet currents, indicating more similar operation in this region. The data of Figures 11-16 are consistent with the viewpoint that anodes in a multipole thruster generate electric fields that reflect at least some of the ions that reach the walls. This viewpoint is shown most clearly by comparison of original and corner only configurations. The minimum magnetic barrier to primary electrons is found in the same corner location for both configurations, but the losses are substantially lower with the all-anode original configurations. The comparison of the original and corner out configurations is less clear cut. The corner out configuration is best at low magnet currents because the rapid loss of primary electrons to the corner anodes is prevented, but this effect does not involve ion reflection. At higher magnet currents, the higher primary-electron loss of the original configuration is apparently balanced by the reduced ion reflection of the corner out configuration.

The apparent reflection of ions at the walls of the multipole ion chamber used herein indicates that there are probably detailed anode and pole piece geometries (apart from corner effects) that should be investigated. Further, the optimization of these geometries should yield further performance improvements.

CHAMBER LENGTH

The effects of ion-chamber length on performance were investigated. Lengths of 2.5, 5.1, 7.6, and 10.2 cm were used with argon, while lengths of 2.5, 5.1, and 7.6 cm were used with xenon. The magnet current was near optimum (10 amperes) for both propellants.

Ion-chamber performance is shown in Figure 17 for argon. Although performance data were obtained over a range of propellant flows with each chamber length, data for all chamber lengths were available only for the flow rate shown. Shorter chambers operated at higher flows, while longer chambers operated at lower flows. For the range of utilization investigated, discharge losses decreased as the chamber length was decreased from 10.2 to 5.1 cm. At 2.5 cm, however, the discharge losses increased.

To obtain some insight into the trends of Figure 17, neutral loss rates were calculated for the 4 chamber lengths using the method of Kaufman and Cohen[12] with a numerical value from the center of the scatter band given therein. This method gives a single neutral loss rate that should correspond to the "knee" of the utilization vs. discharge loss curve. For argon in 2.5, 5.1, 7.6 and 10.2 cm chambers, the predicted neutral loss rates were 0.82, 0.52, 0.40, and 0.36 amperes equivalent. The multipole design is believed to have a more efficient primary-electron region than the usual divergent-field thrusters (such as SERT II). Because of this, the experimental neutral loss rates would be expected to be the same as, or less than, the calculated values. The normal tendency when shortening an ion chamber is to decrease both the maximum utilization and the minimum discharge loss. Compared to the propellent flow rate of 1.00 ampere equivalent, the predicted

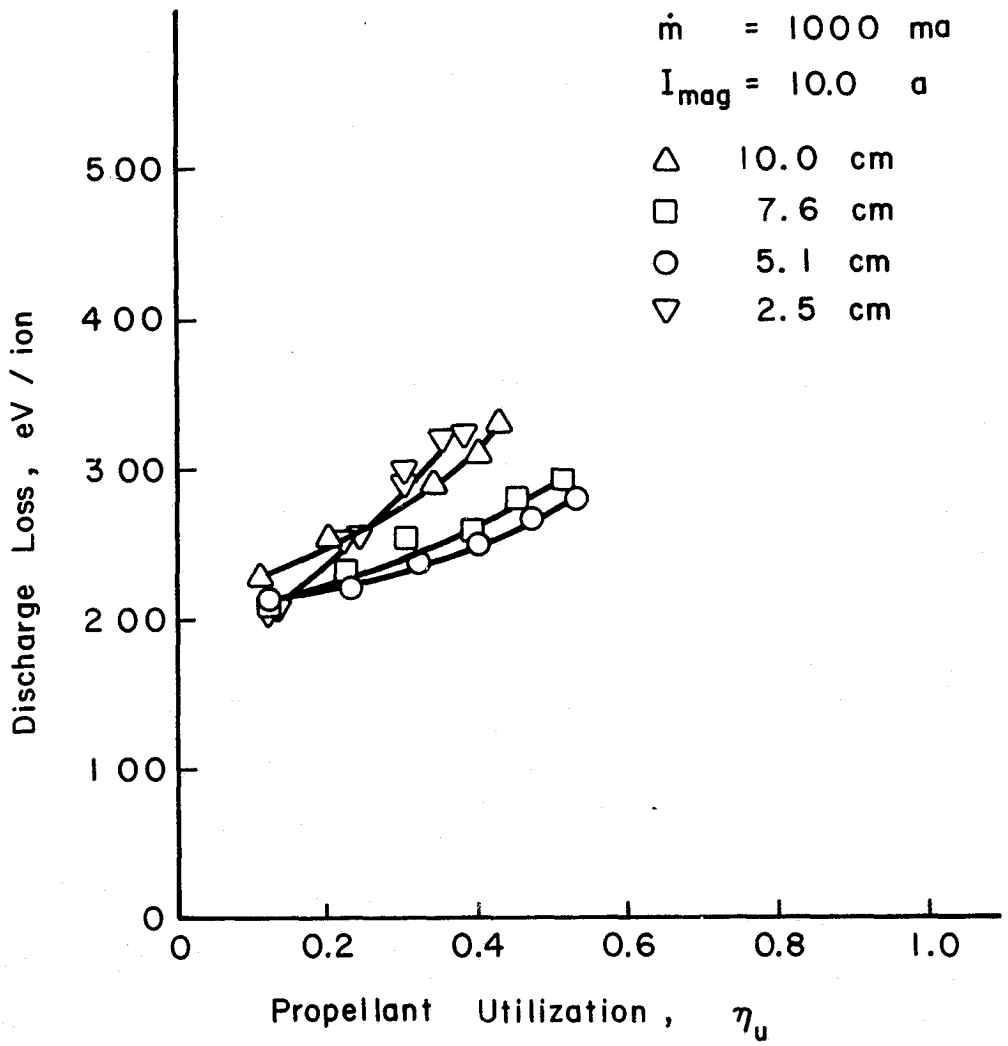

Figure 17. Effect of chamber length on discharge-chamber performance with argon propellant.

neutral loss rate is perhaps small for chamber lengths of 5.1-10.2 cm. In this range of chamber lengths and the range of utilizations covered, then, the decrease in minimum discharge loss should be most noticeable. For the 2.5 cm chamber, though, the predicted neutral loss is so large that the rise in losses near the knee would be expected to show in much of the utilization range covered. Hence the observed rise in losses for this length should be expected.

The cathode emission limit of roughly 3 amperes prevented the approach of knee utilizations with longer chamber lengths. Otherwise, the reasoning given above would lead to the expectation of several cross-overs in discharge-loss curves. In other words, each chamber length would be expected to have the lowest losses at some utilization, the level of this utilization increasing in some manner with chamber length.

Beam profiles were obtained 6.5 mm downstream of the accelerator system and are shown in Figure 18. The beam profiles are quite uniform for all chamber lengths, but are least uniform for the shorter lengths (as indicated by the flatness parameters). From the viewpoint of wall losses alone, the shorter chambers would be expected to have flatter profiles. That is, the losses to the side (cylindrical) walls should cause nonuniform ion densities, and hence nonuniform ion beam profiles. These side wall losses become a smaller fraction of total wall losses for shorter chambers, hence the profiles should be flatter. The fact that the beam profiles become less flat with the shorter chambers indicates that wall losses are not the only significant parameters. As will be shown by probe data, cathode placement and corner effects of the multipole chamber are probably also important.

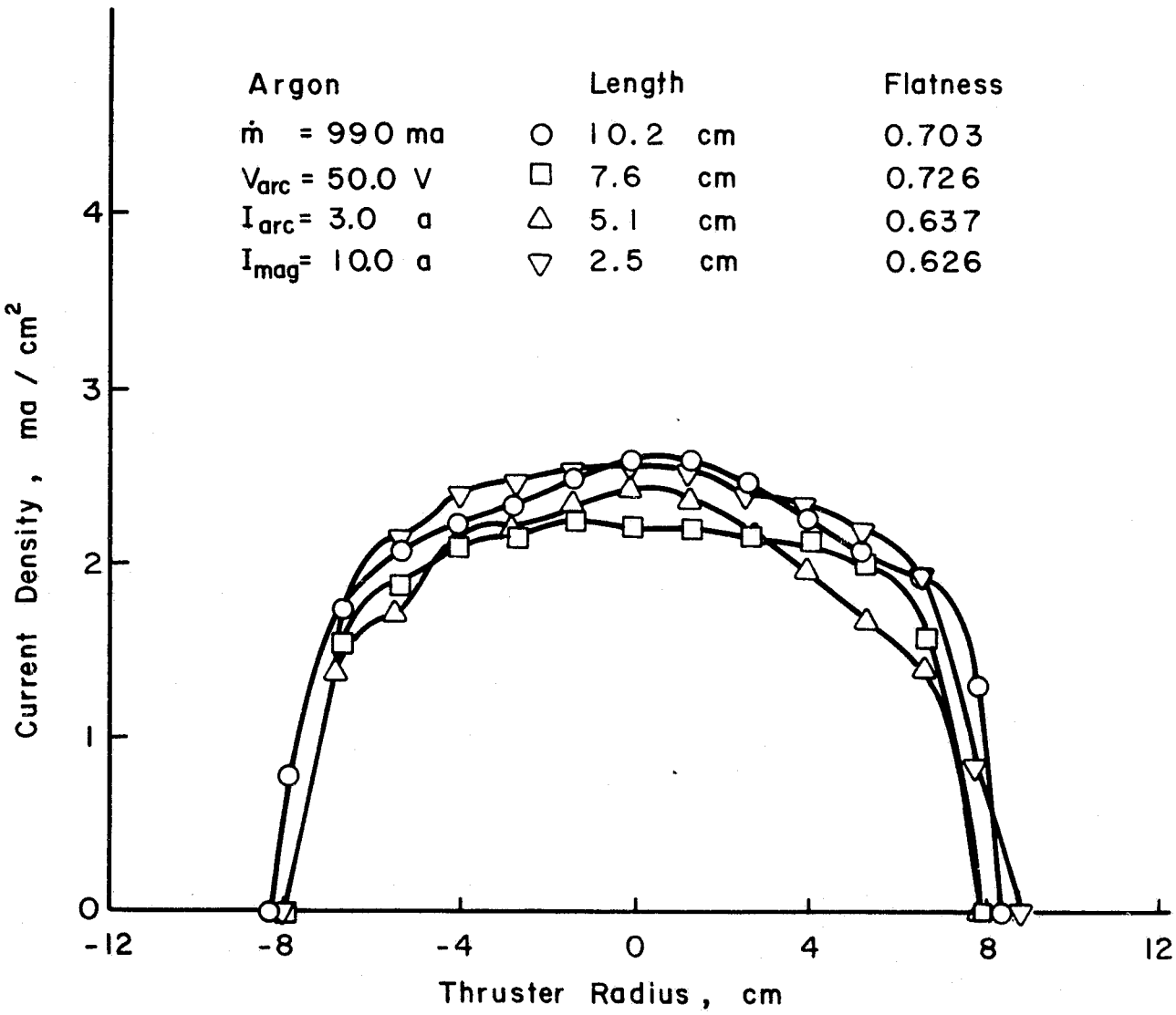

Figure 18. Effect of chamber length on ion-beam profile with argon propellant.

Plasma properties within the ion chamber were obtained using a moveable Langmuir probe. Data were obtained for the 5.1 cm chamber (Figure 19) and the 7.6 cm chamber (Figure 20). Plasma potential, Maxwellian temperature and primary and Maxwellian densities are shown for both chamber lengths. The locations of the various pole pieces and anodes are also indicated. The cathode and its support occupied the open region on the centerline of the upstream end of the chamber.

Plasma properties were reasonably uniform throughout both ion chamber volumes. Rises in most properties were evident near the axis of the upstream end of the chambers. These rises were due to the proximity of the refractory metal cathode. Both the primary and Maxwellian electron densities show general decreases at the outer radius of the upstream end of the chamber. These decreases may be due to the higher losses of the corner anodes. If so, however, it is not clear why the primary electron density should be lower downstream of the corner than it is at the corner anode. In any event, the primary and Maxwellian electron densities approximate cause and effect for ion production. The non-uniformities of these parameters at the upstream end of the chamber are consistent with the decreased ion-beam flatness as the chamber is shortened from 7.6 to 5.1 cm (Figure 18).

With xenon the discharge losses decreased with chamber length over the range investigated. The comparison is shown in Figure 21 for a propellant flow of 440 ma equivalent, but the same trend was also found for 220 and 660 ma equivalent. Note that no increase in losses was found for the 2.5 cm chamber over the range of utilization. This difference from argon performance is probably due to the lower neutral

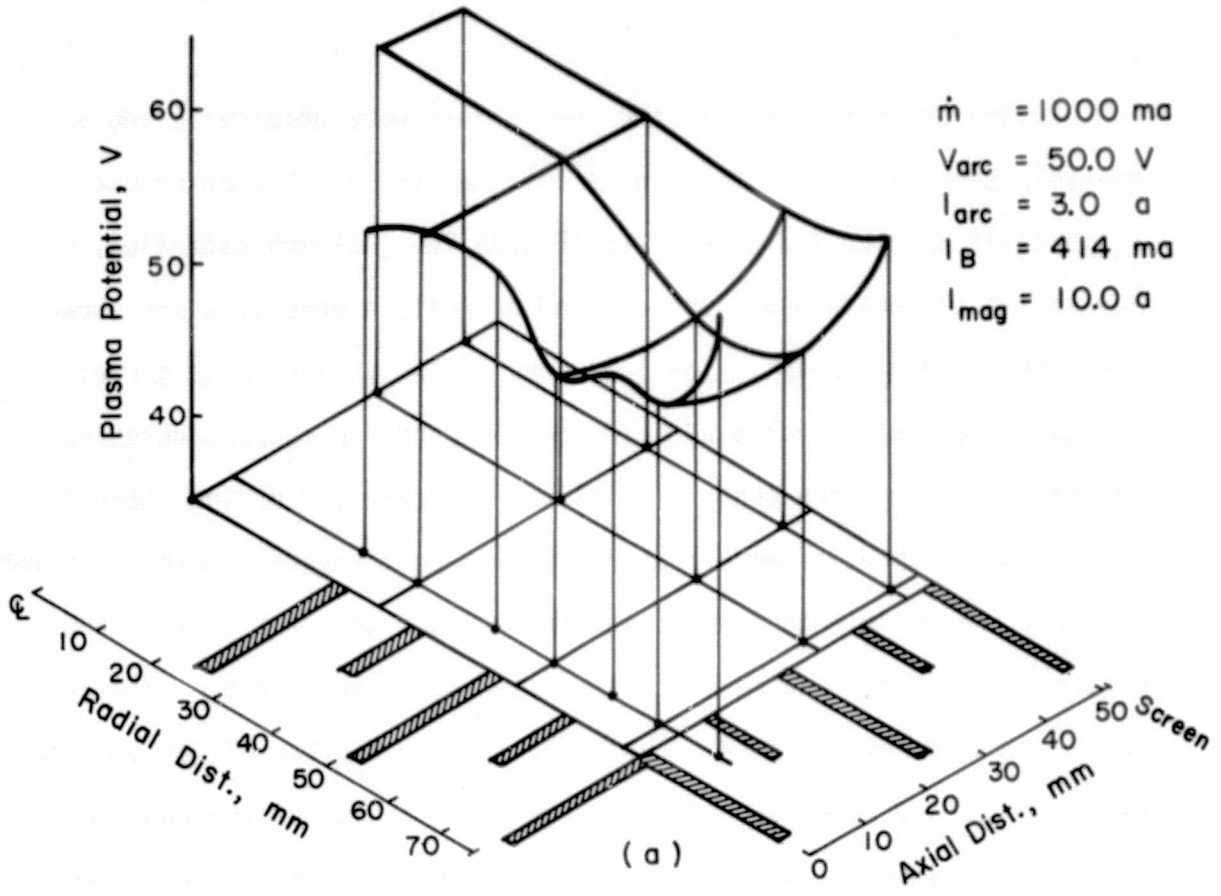

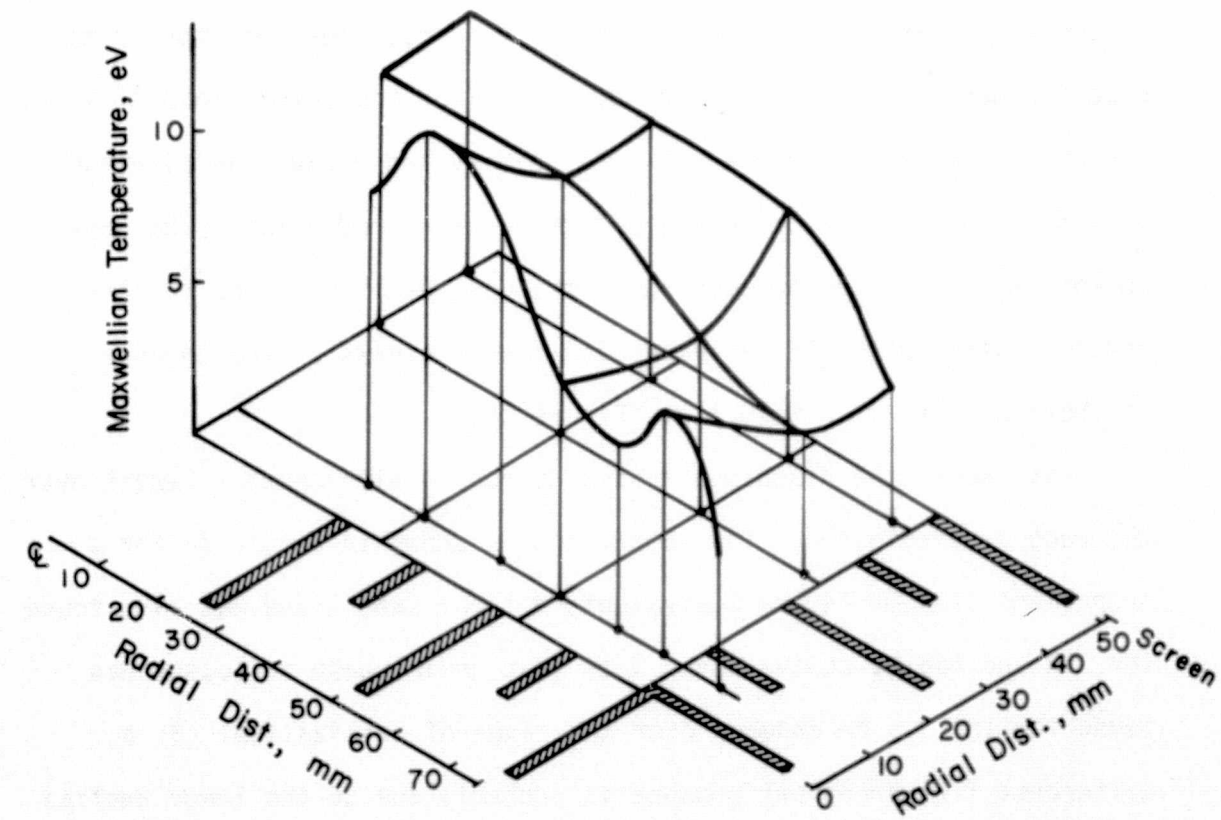

Figure 19. Plasma properties for 5.1 cm chamber length with argon propellant.

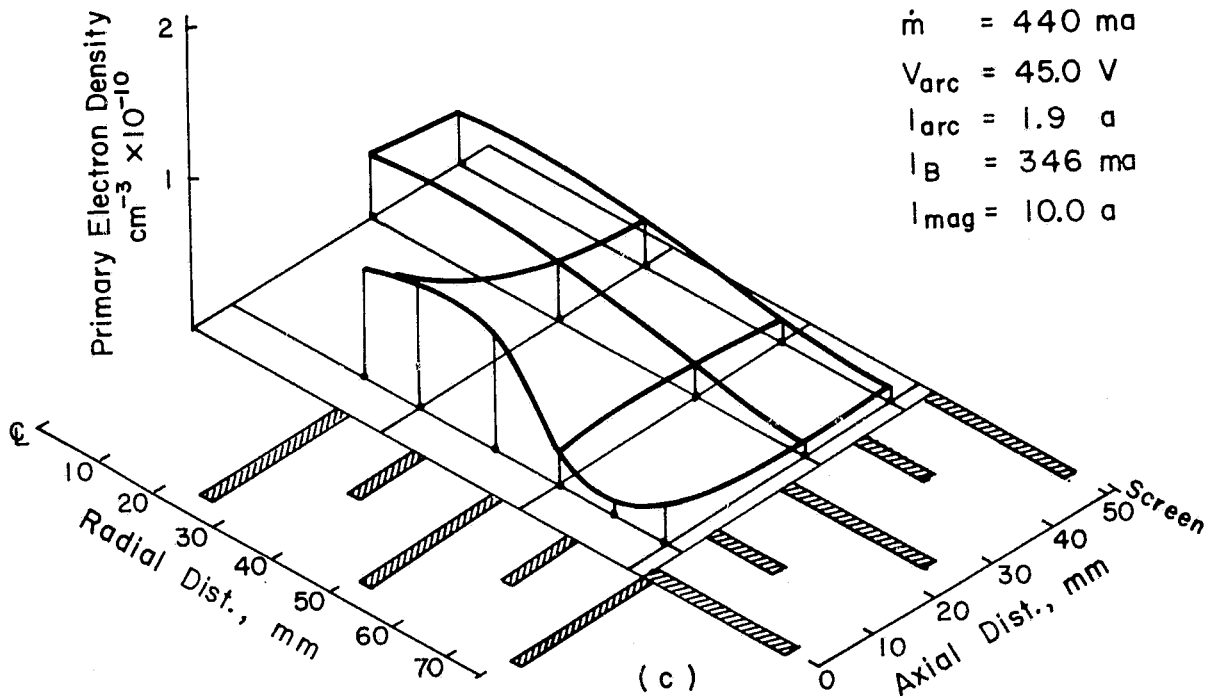

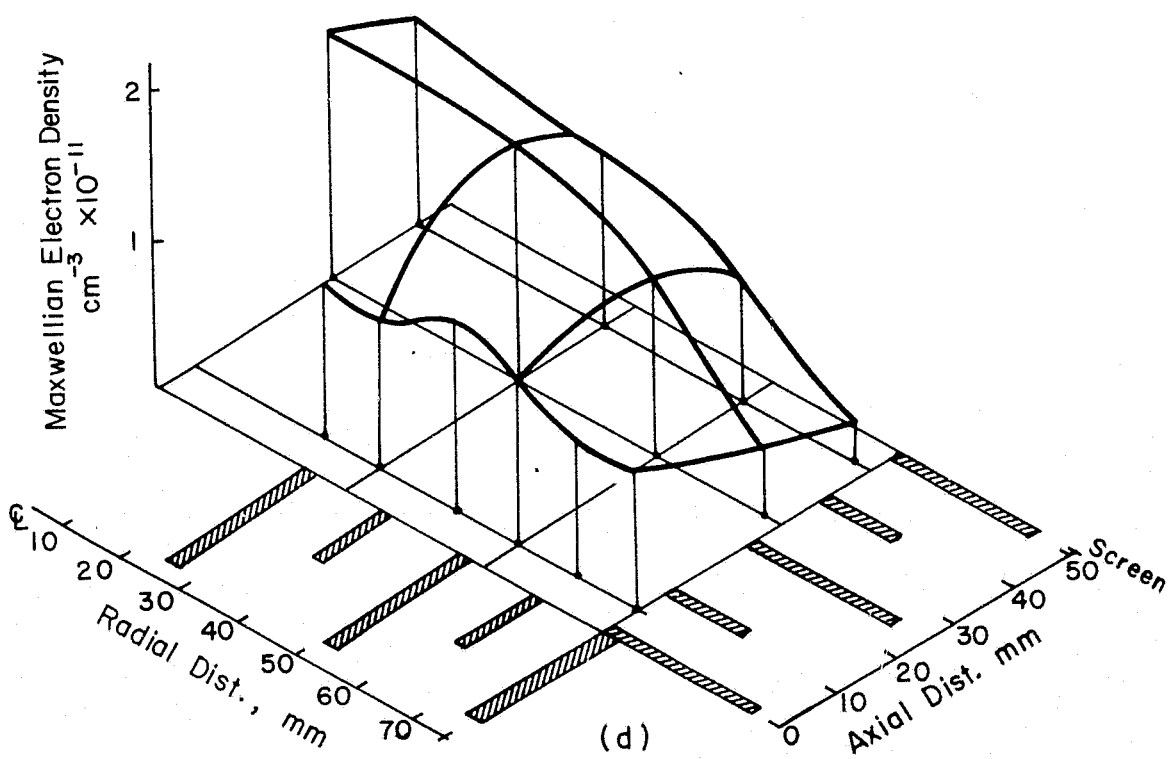

Figure 19 concluded.

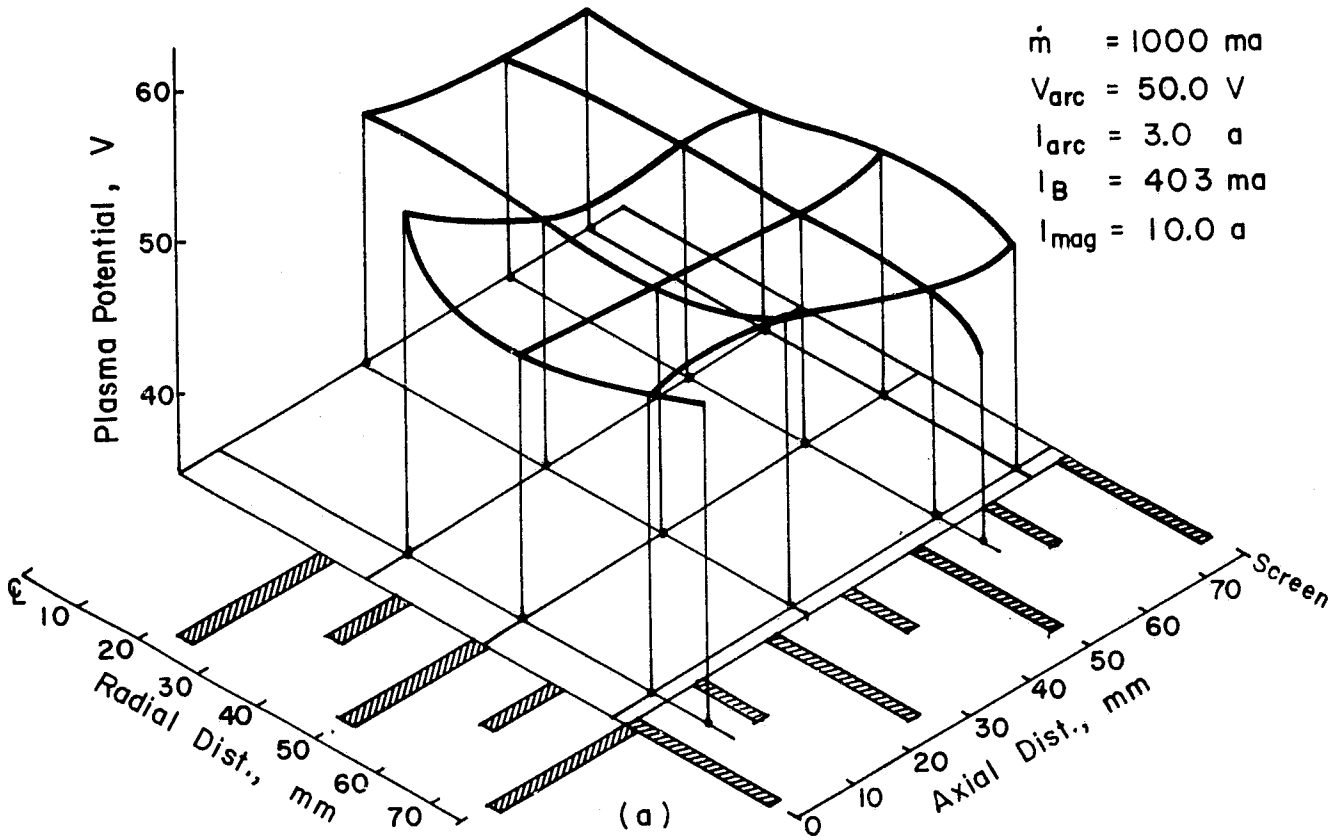

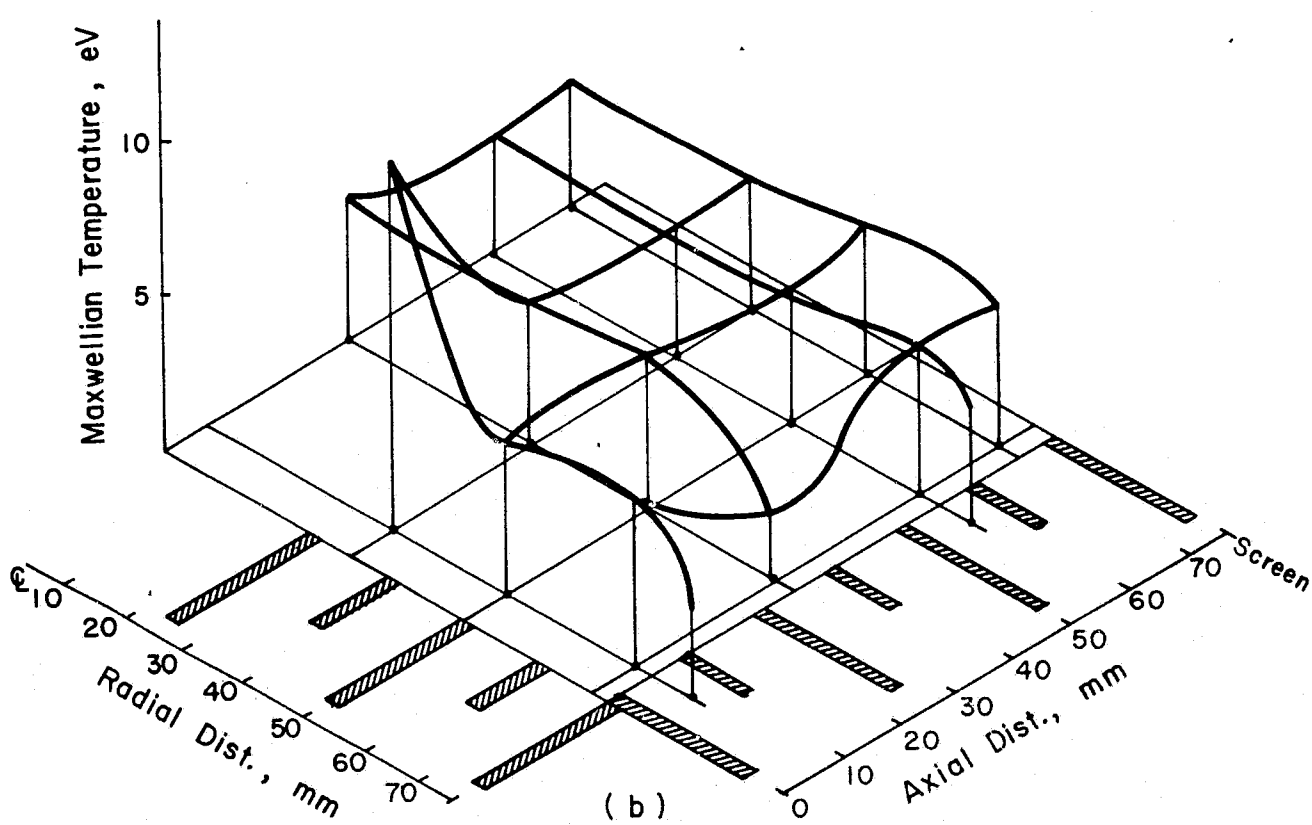

Figure 20. Plasma properties for 7.6 cm chamber length with argon propellant.

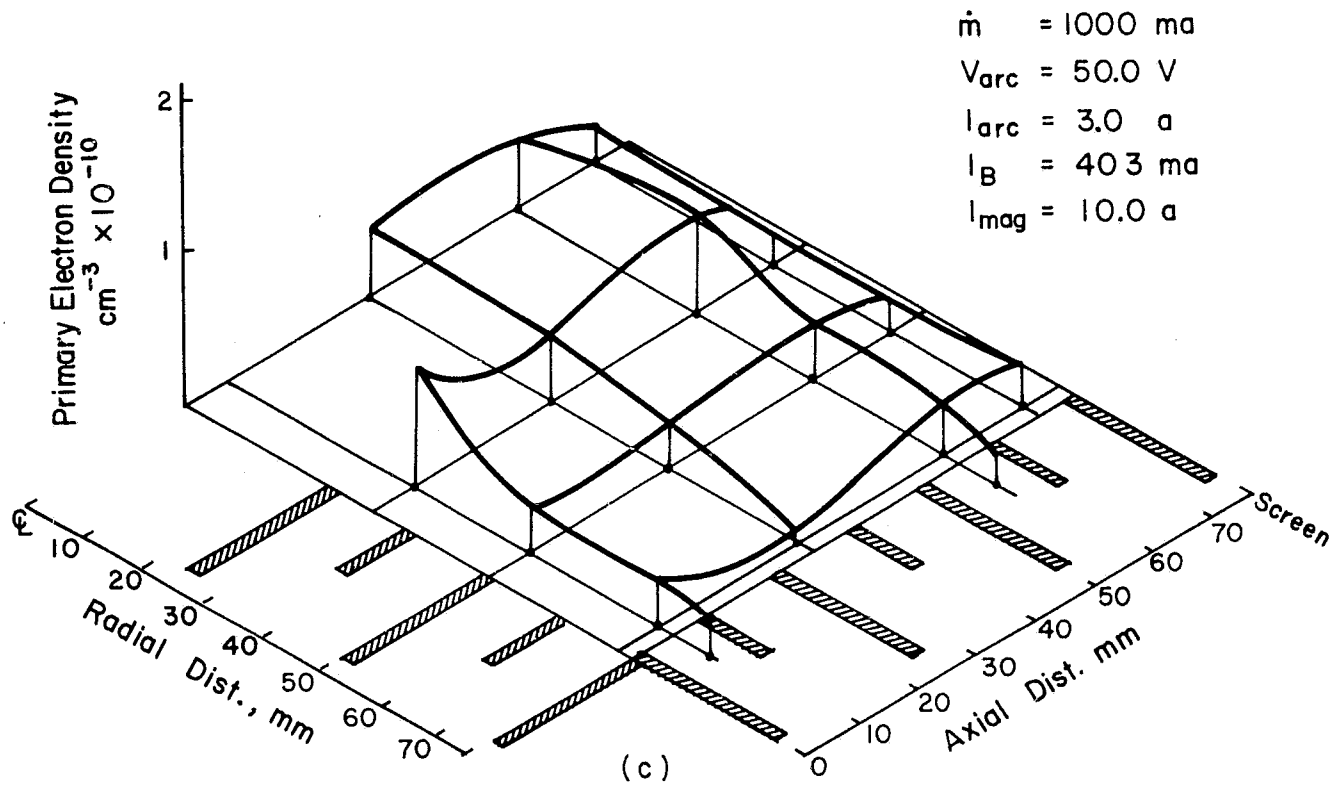

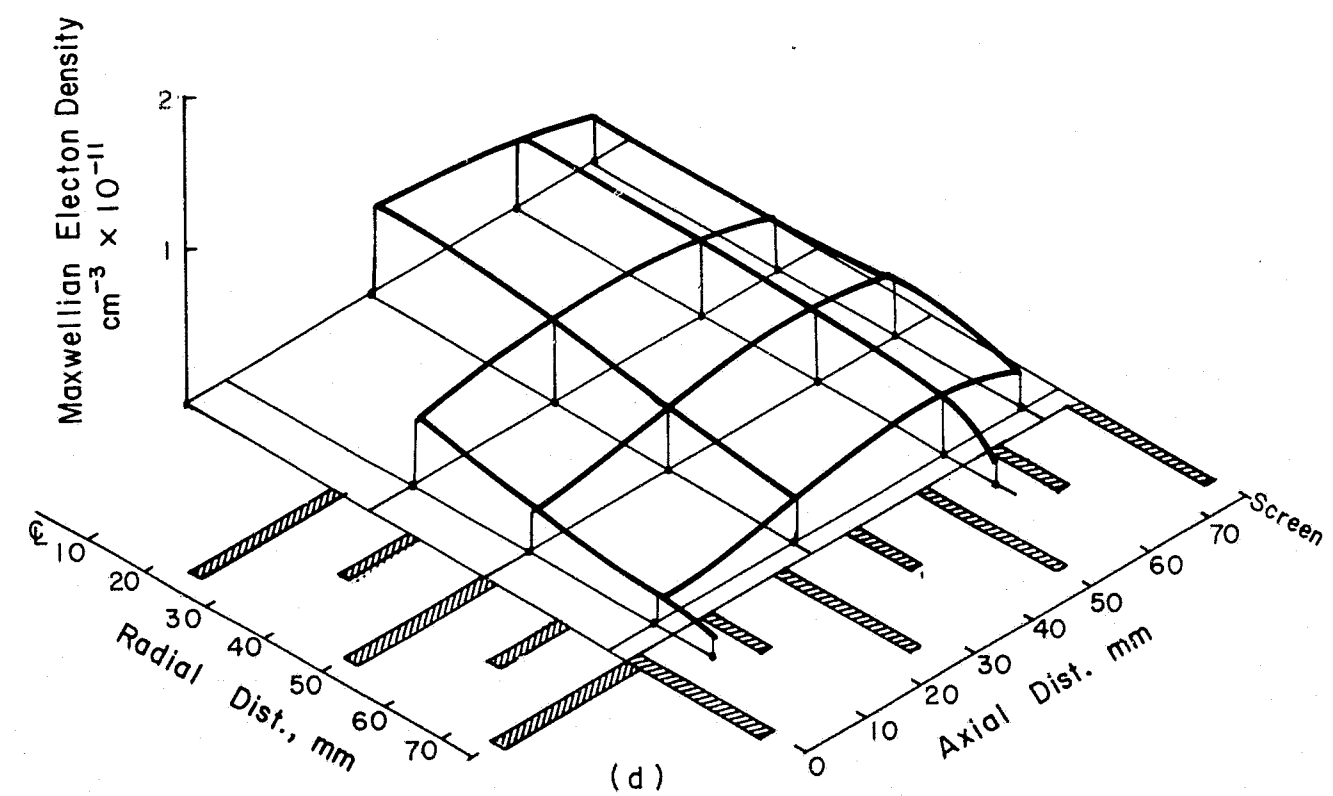

Figure 20 concluded.

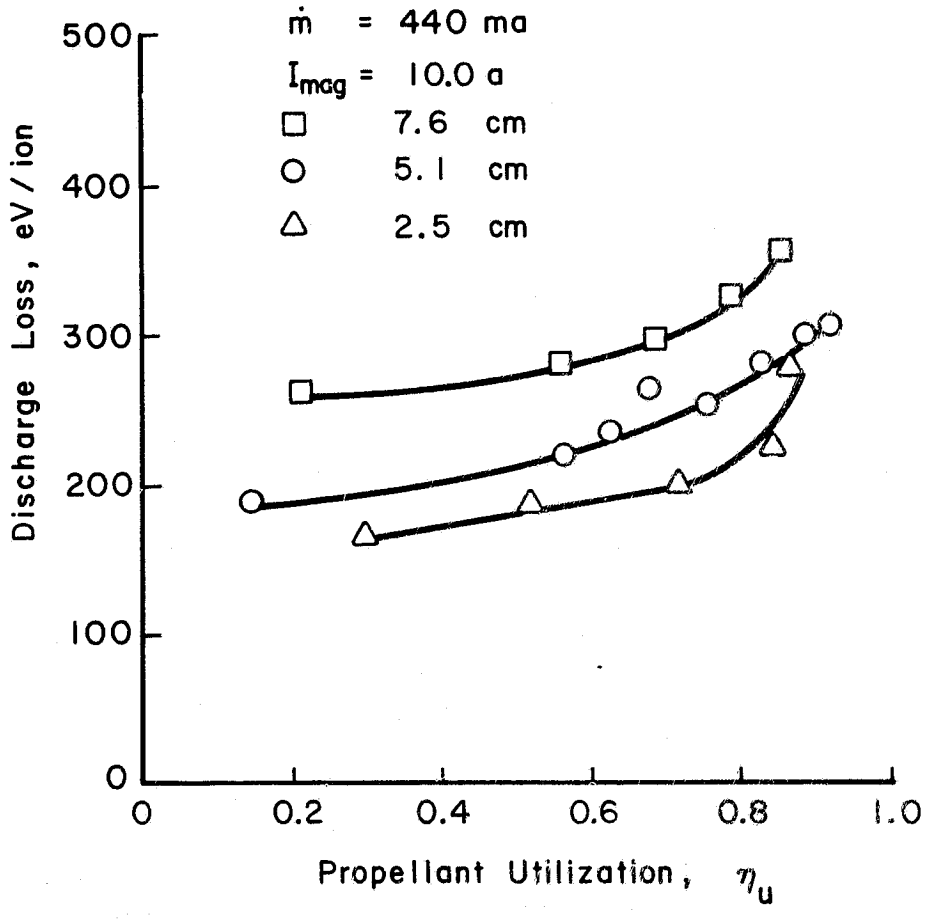

Figure 21. Effect of chamber length on discharge-chamber performance with xenon propellant.

losses with xenon. Using the same procedure as with argon, the predicted loss rates were 0.15, 0.094, and 0.074 amperes for chamber lengths of 2.5, 5.1, and 7.6 cm. For a propellant flow rate of 440 ma equivalent, these neutral loss rates correspond to knee utilizations of 0.66, 0.79, and 0.83. These predicted knee utilizations appear in rough agreement with the experimental values. The corrections for doubly ionized propellant atoms and propellant backflow from the vacuum facility amounted to a total of about 10 percent in the xenon utilization, so that disagreement of predicted knee utilizations with experimental data is perhaps within the uncertainty in utilization.

Xenon beam profiles are presented in Figure 22 for the three chamber lengths. The profiles for both the 2.5 and 7.6 cm lengths are very uniform, but the profile for the 5.1 cm length is much less uniform. As with the argon profiles, Langmuir probe data from the ion chamber can be used to explain some of the trends.

Plasma properties within the ion chamber are shown in Figure 23 for the 5.1 cm length and in Figure 24 for the 7.6 cm length. The radial variations in plasma properties at the upstream end of the chamber are similar to those shown in Figures 19 and 20 for argon. The cathode and high corner losses are again believed to be the cause of these variations. The decreased uniformity in going from the 7.6 to the 5.1 cm chamber is consistent with Maxwellian electron density changes near the accelerator system in Figures 23 and 24. (The ion density roughly equals the density of Maxwellian electrons.) The variation near the center of the 5.1 cm profile in Figure 22 is not typical, and may have been the result of an electrical transient.

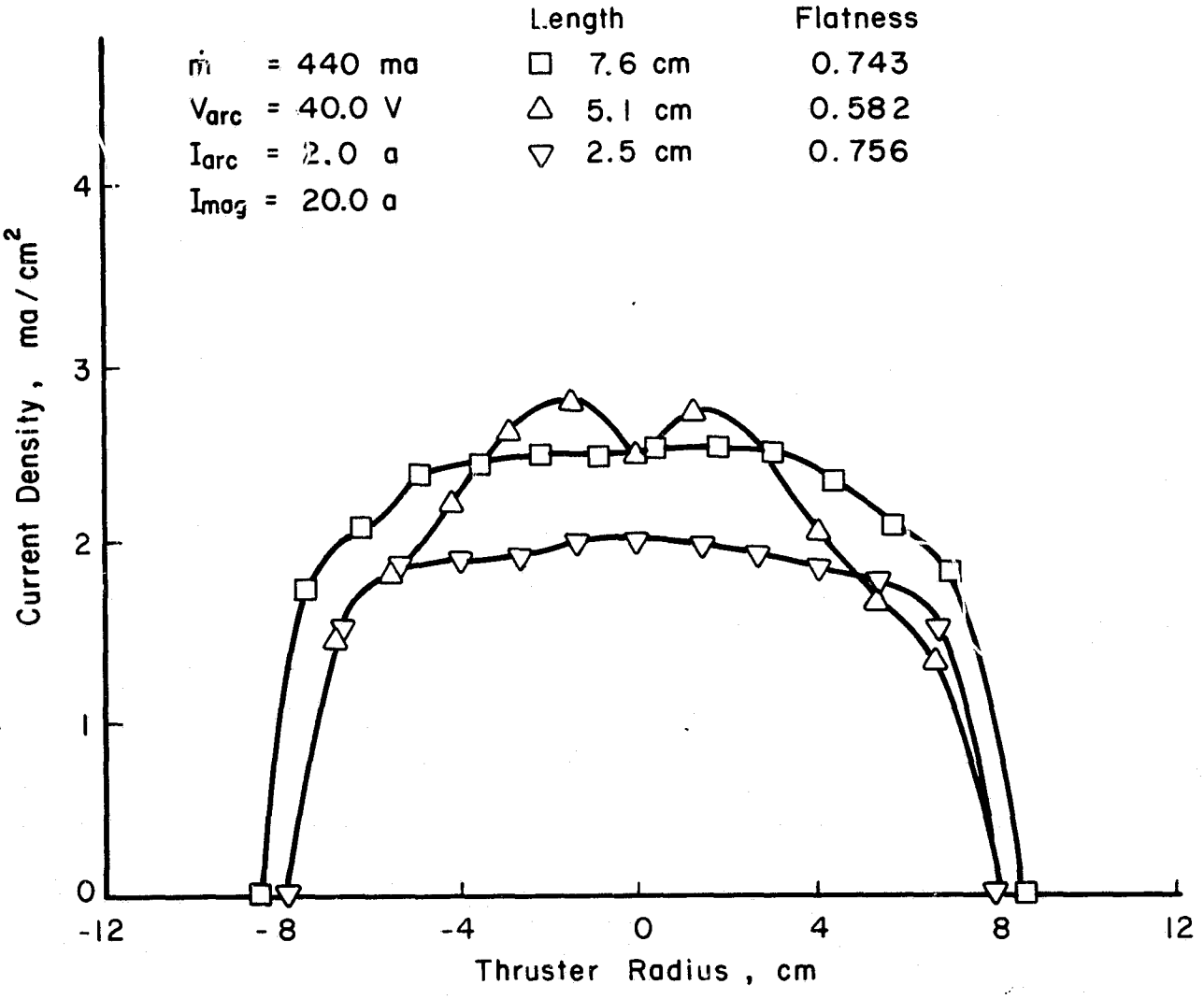

Figure 22. EFFECT OF CHAMBER LENGTH ON ION-BEAM PROFILE WITH XENON PROPELLANT.

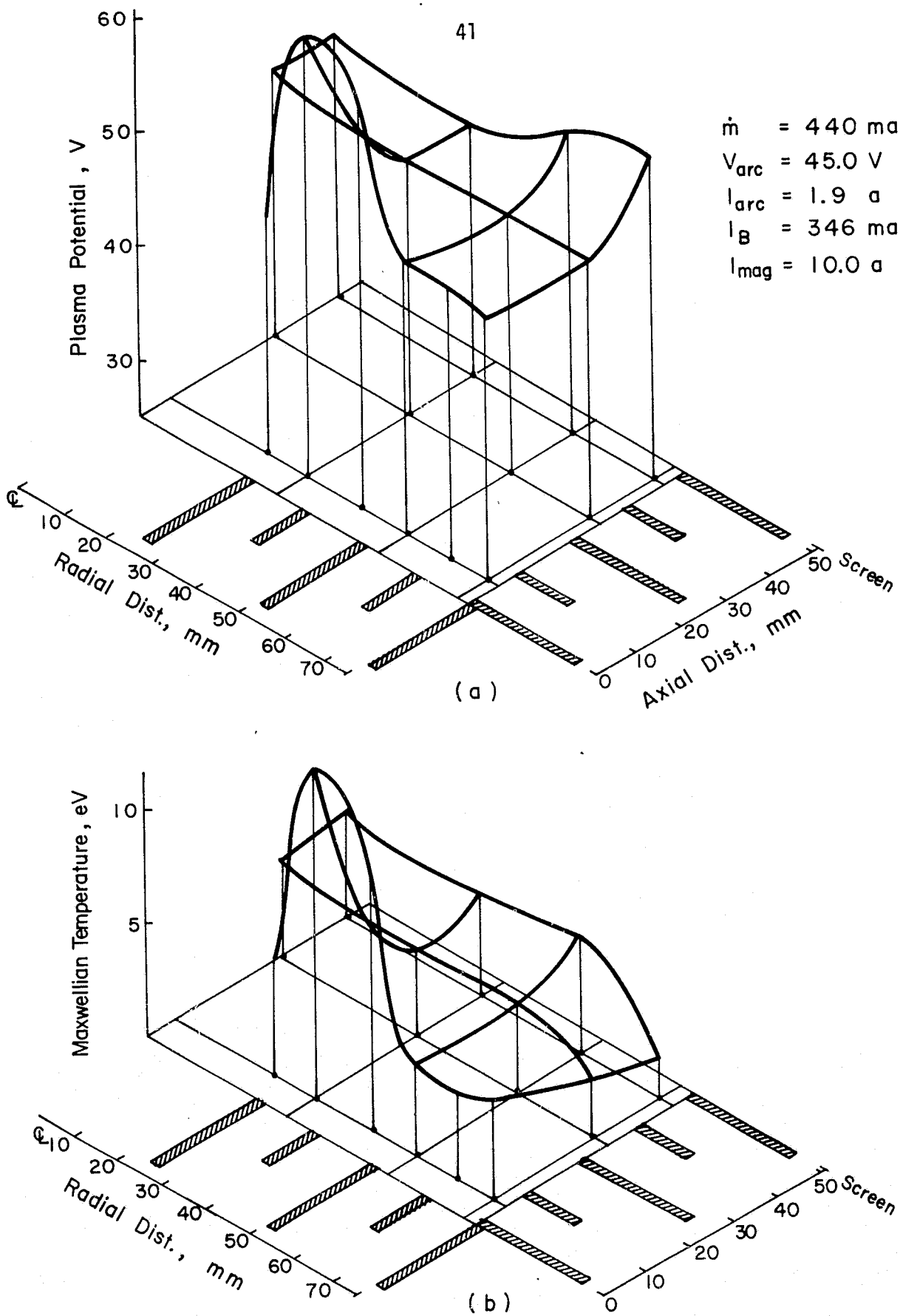

Figure 23. Plasma properties for 5.1 cm chamber length with xenon propellant.

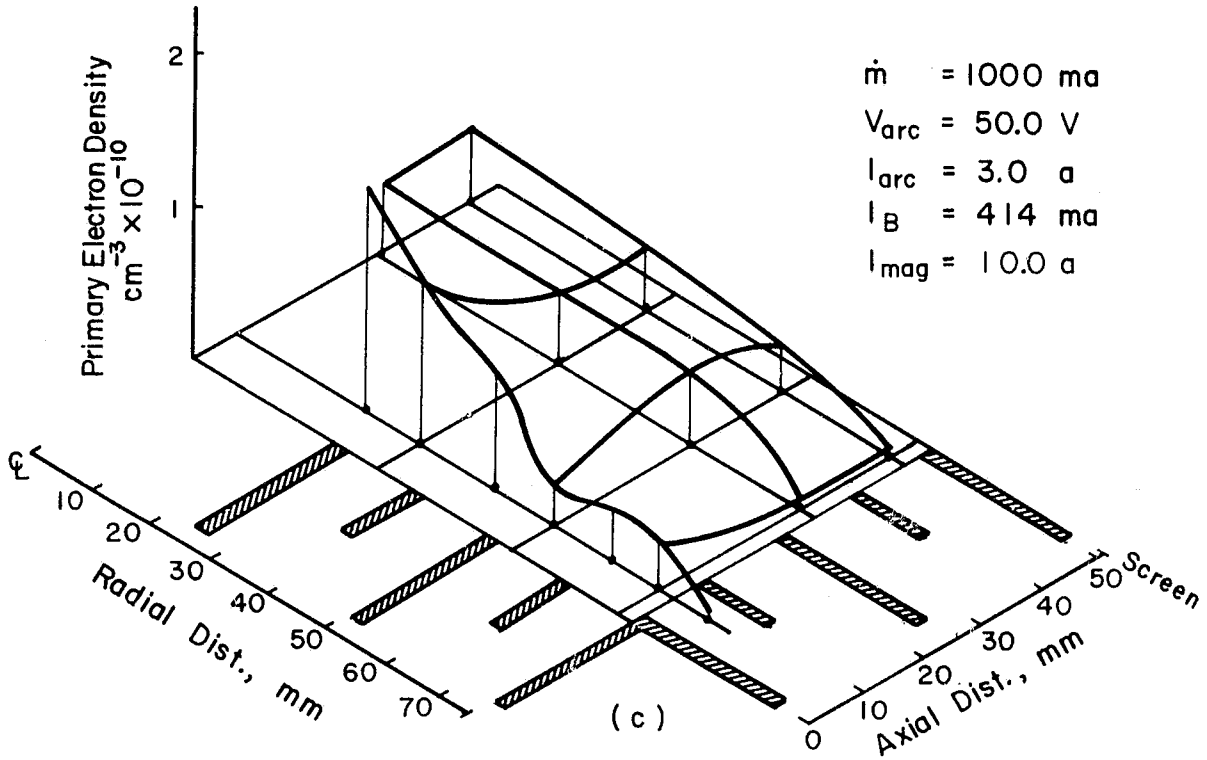

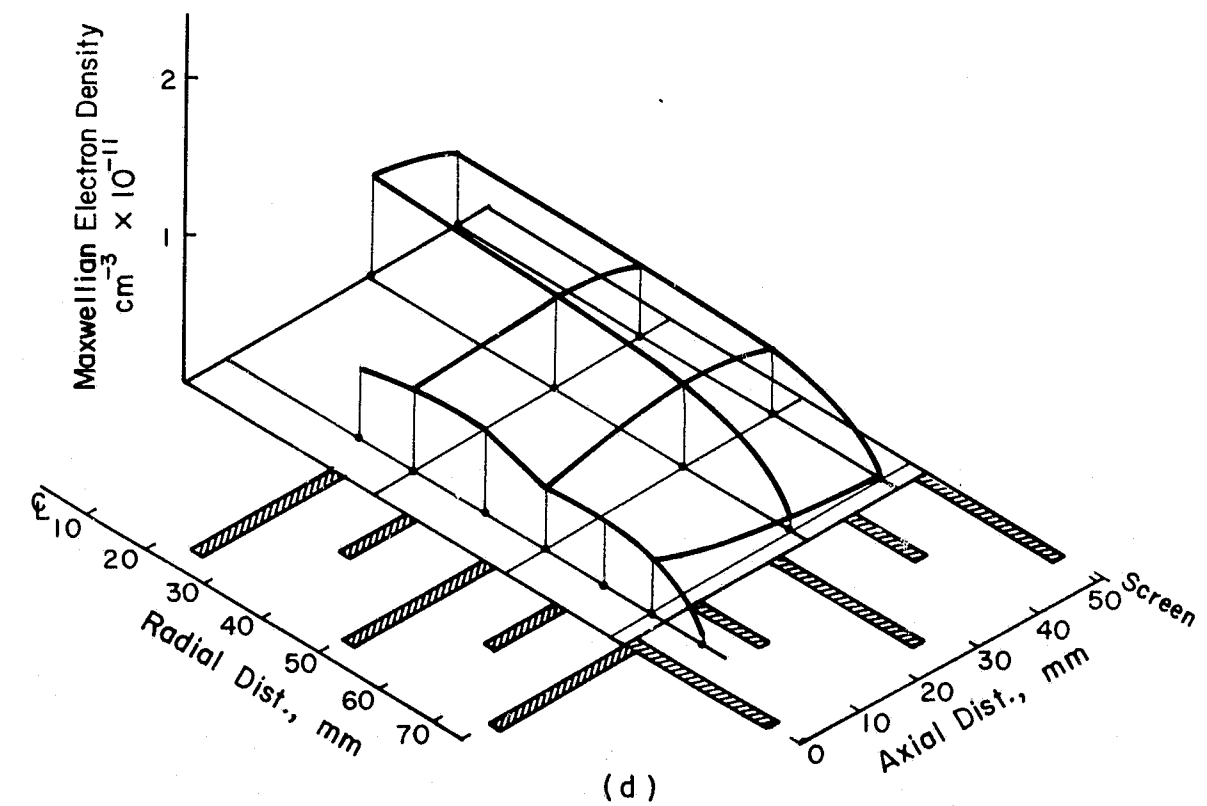

Figure 23 concluded.

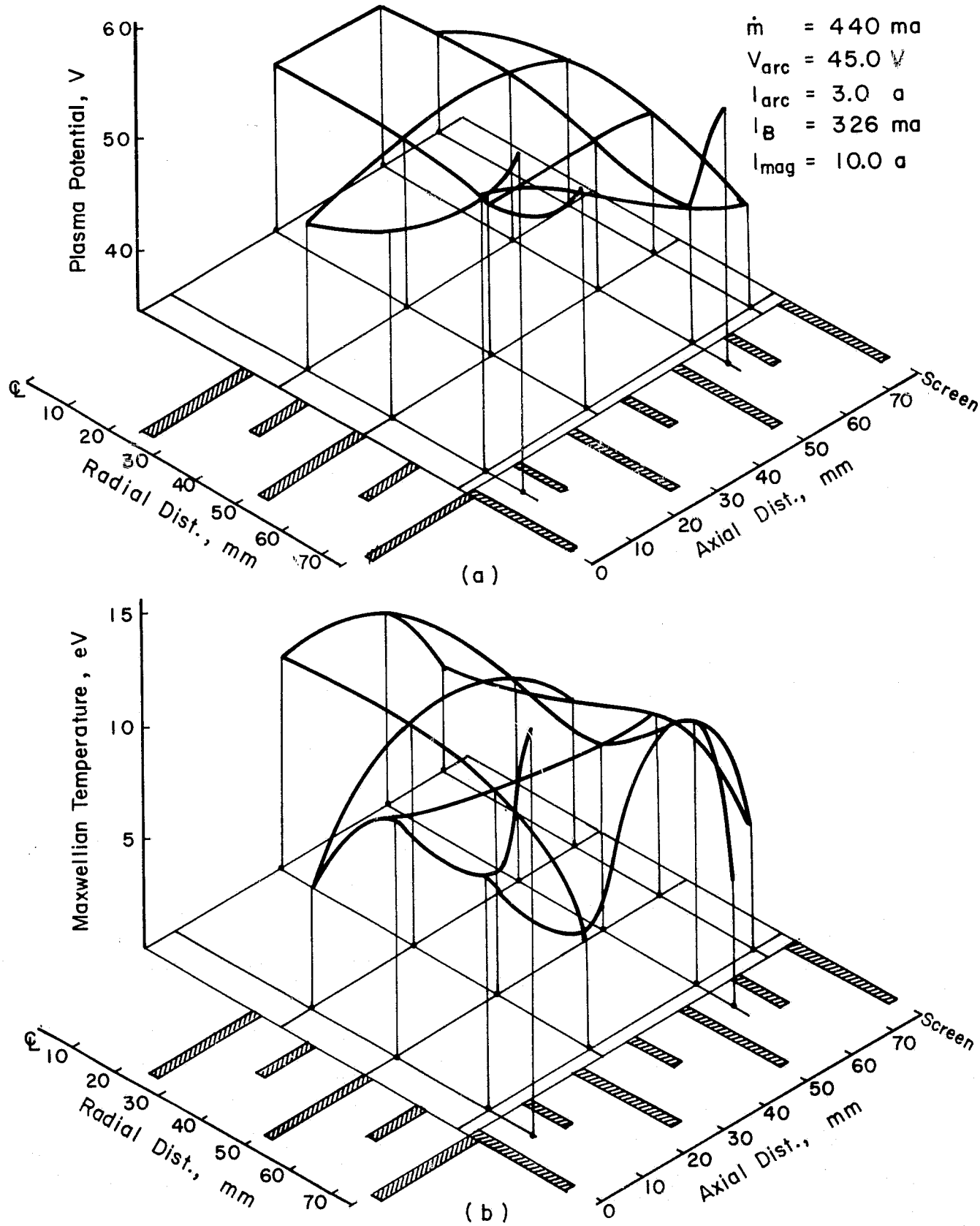

Figure 24. Plasma properties for 7.6 cm chamber length with xenon propellant.

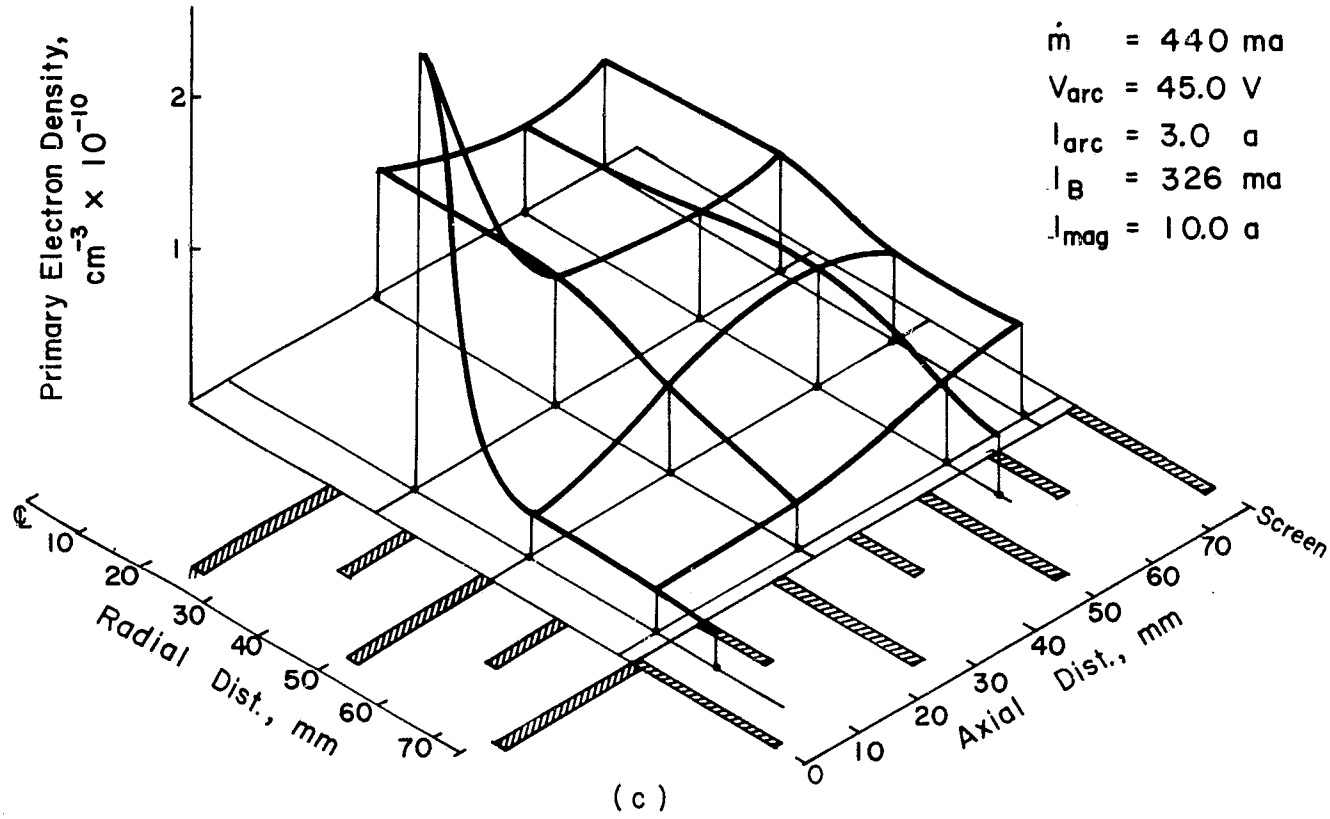

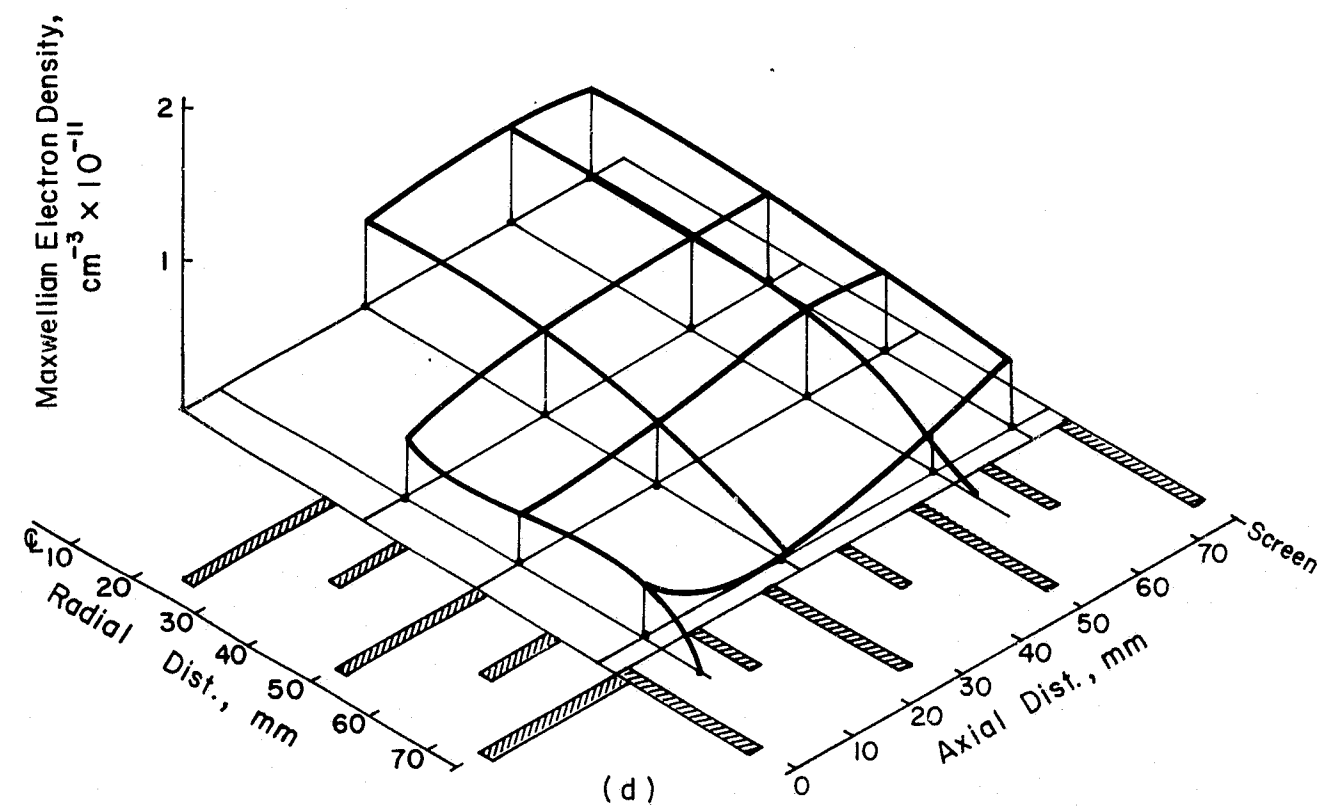

Figure 24 concluded.

The profile for the 2.5 cm chamber does not agree with the trend established by the 7.6 and 5.1 cm profiles, although the latter are in agreement with measured plasma properties. A Langmuir probe survey is not available for the 2.5 cm length, so a comparison cannot be made with plasma properties inside the ion chamber. It should also be noted that the 2.5 cm profile in Figure 22 also does not agree with the 2.5 cm profile for argon in Figure 18. These apparent inconsistencies cannot be explained at the present time.

THROTTLING

The effect of varying the propellant flow rate on thruster performance was investigated using the 7.6 cm long chamber for both argon and xenon. Data were obtained over approximately a 3:1 range for both propellants. Data obtained with argon, Figure 25, show essentially the same performance for the 660 and 1000 ma equivalent flows. Slightly higher losses are shown for some of the utilization range with the 1735 ma equivalent flow. In all cases the minimum losses are in the 200-250 ev/ion range. Using the procedure described earlier, knee utilizations of 0.39, 0.60, and 0.77 would be expected for the 7.6 cm chamber length operating at the flows shown in Figure 25.

Similar data obtained with xenon are shown in Figure 26. The xenon performance is more dependent on flow, with the lowest flow giving the lowest losses. Minimum discharge losses range from about 150-250 ev/ion. The predicted knee utilizations are 0.66, 0.83, and 0.89.

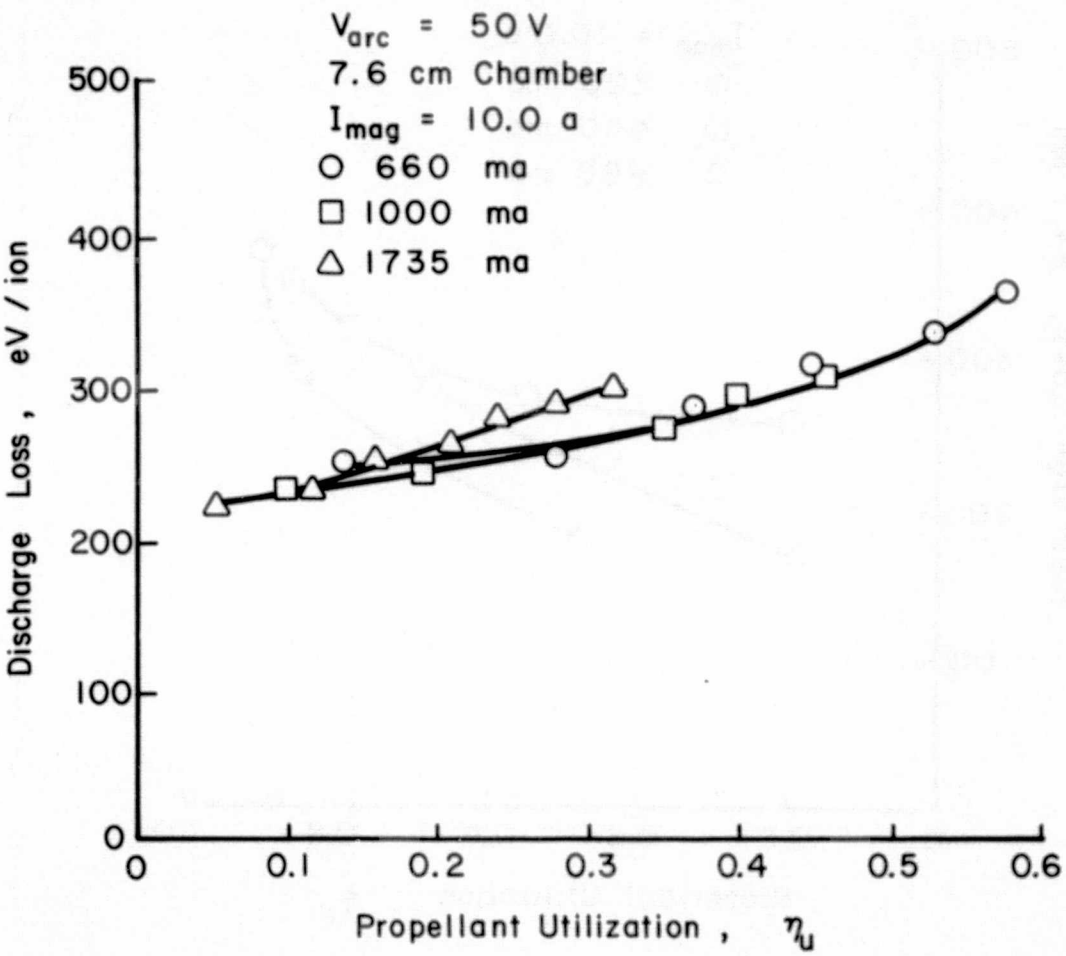

Figure 25. EFFECT OF FLOWRATE ON DISCHARGE-CHAMBER PERFORMANCE WITH ARGON PROPELLANT.

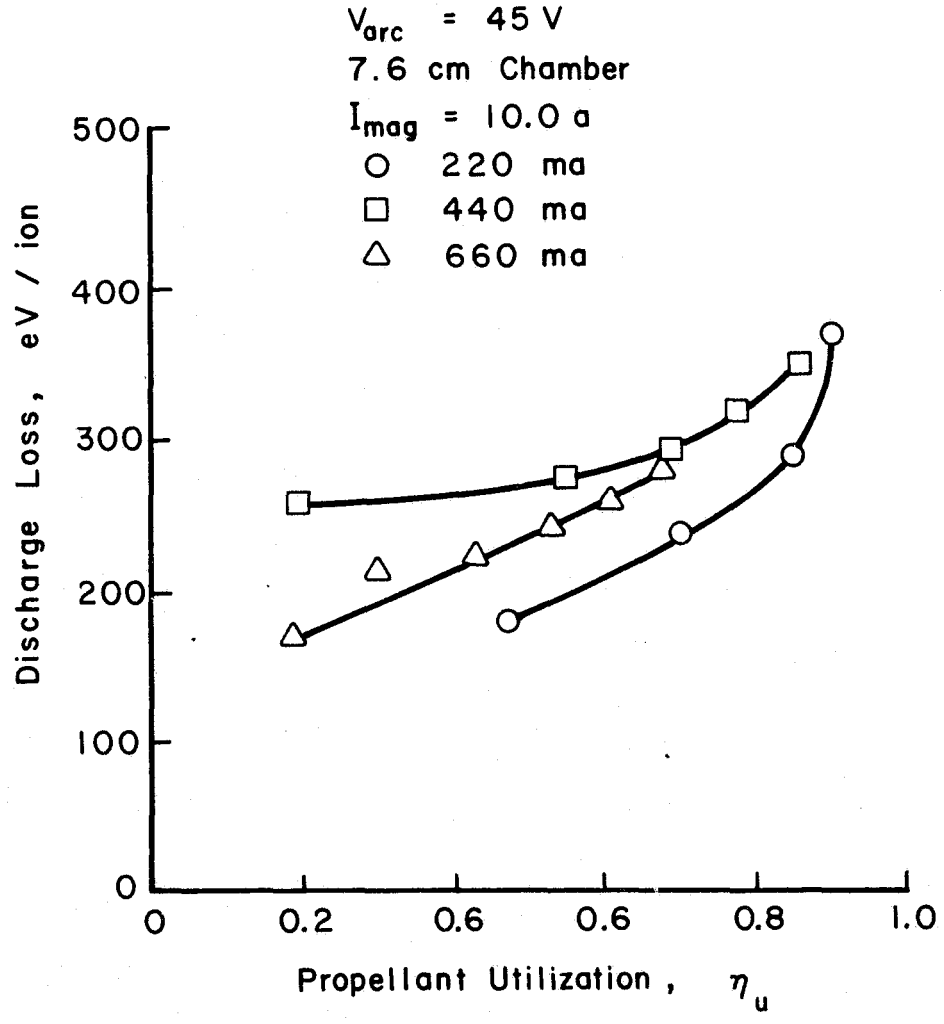

Figure 26. EFFECT OF FLOWRATE ON DISCHARGE-CHAMBER PERFORMANCE WITH XENON PROPELLANT.

DOUBLE IONIZATION

An ExB momentum analyzer was installed near the end of the investigation. Some preliminary data have been obtained using this analyzer with the 7.6 cm long chamber. As mentioned earlier, the analyzer probe was located 60 cm downstream of the accelerator system and was fixed parallel to the beam axis. Data were taken at locations corresponding to 0, 1/4, 1/2, and 3/4 of the thruster radius.

A typical argon trace is shown in Figure 27. Peaks corresponding to A^+ and A^{++} are shown, together with a less typical peak for Xe^+. The latter peak indicates that there was still some xenon present in the feed system and/or vacuum system as the result of xenon operation about an hour earlier. The argon double ionization data are summarized in Figure 28. The ratios of the double-to-single ion currents are shown as a function of thruster radius and discharge voltage for two propellant flow rates. As shown, the fraction of double ionization increases with decreasing flow rate, but the change in utilization that occurs with the flow rate may be as important as the flow rate change.

A typical trace obtained with xenon is shown in Figure 29. The expected peaks for Xe^+ and Xe^{++} are shown along with an Al^+ peak. The Al^+ peaks were smaller than the Xe^{++} peaks, but were present in all traces. In comparison, no Al^+ peaks were observed while using argon propellant. The aluminum is assumed to come from the anodes, which were the only aluminum thruster components.

The xenon double ionization data are summarized in Figure 30. The fraction of double ionization again increases with discharge voltage, although the general level of double ionization was higher than with argon.

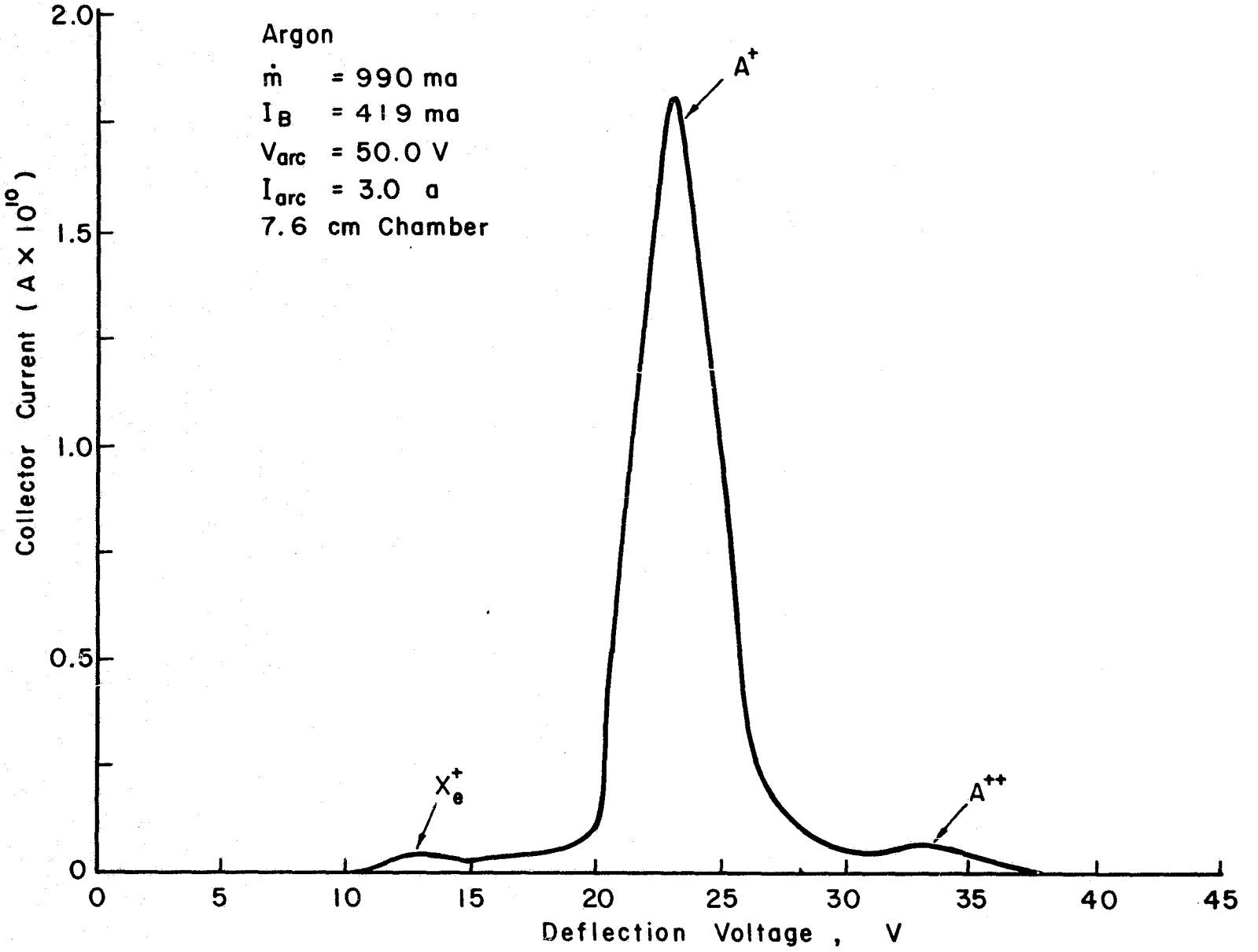

Figure 27. Typical trace from ExB mass analyzer for argon propellant.

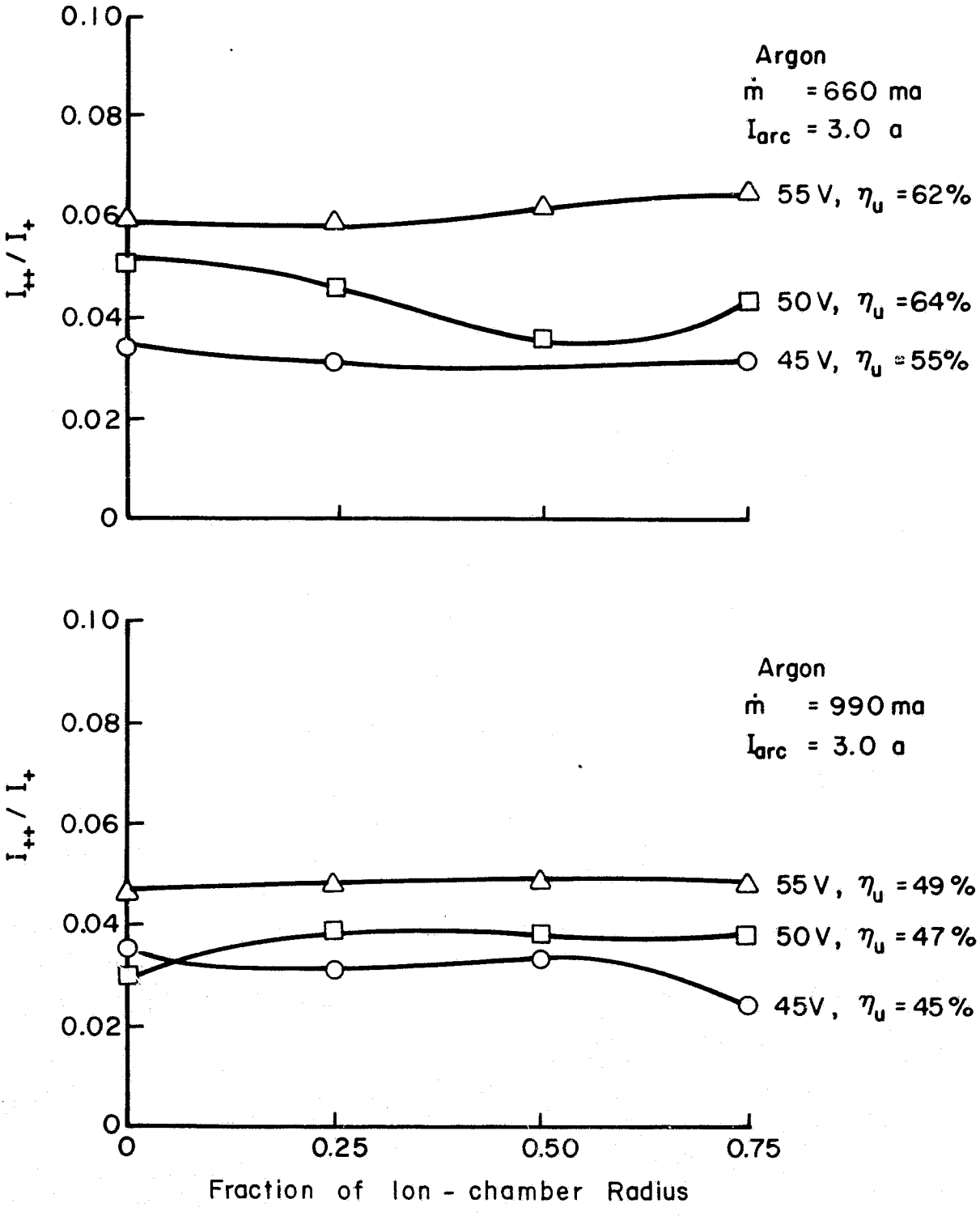

Figure 28. Fraction of doubly ionized argon for various operating conditions.

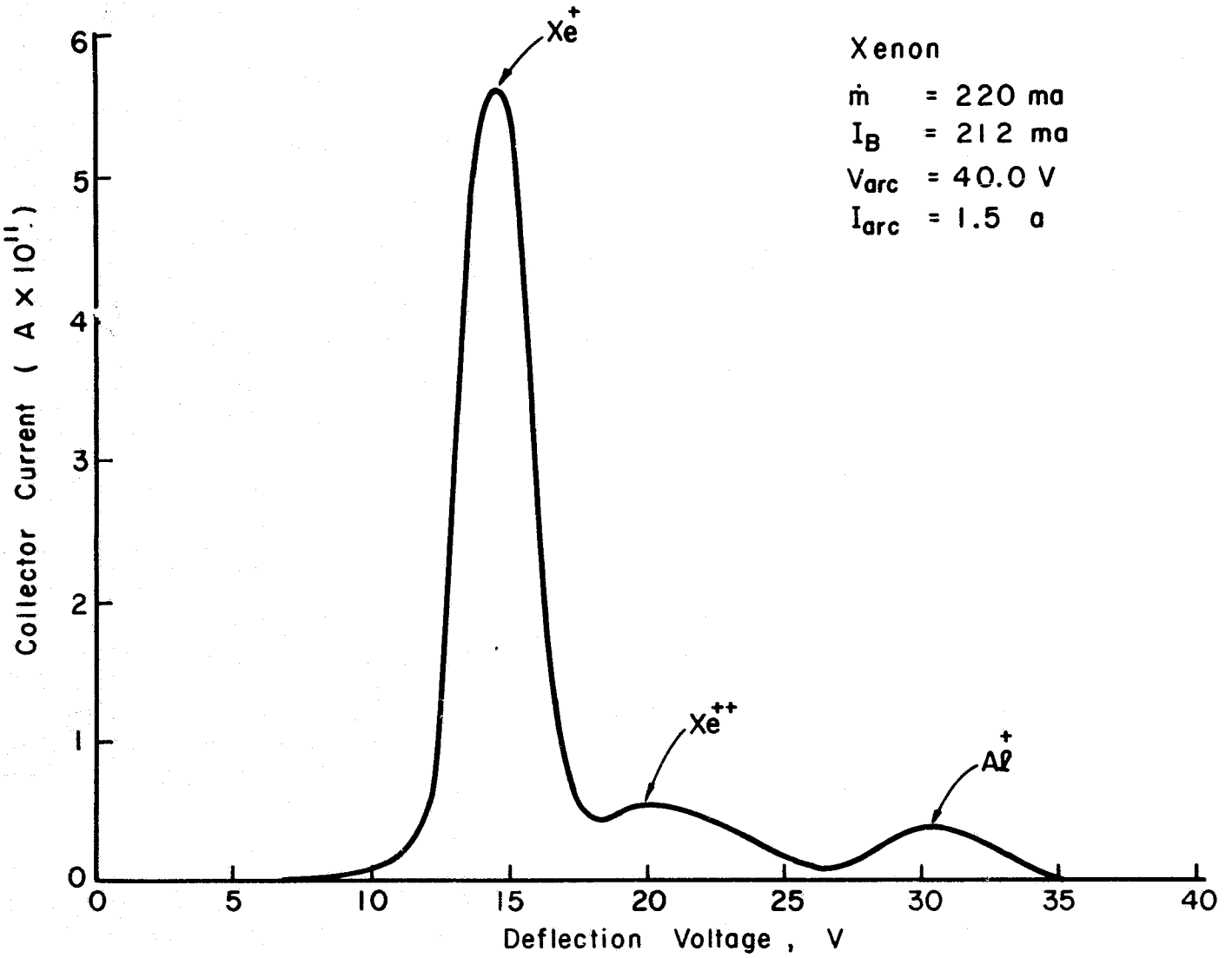

Figure 29. Typical trace from ExB mass analyzer for argon propellant.

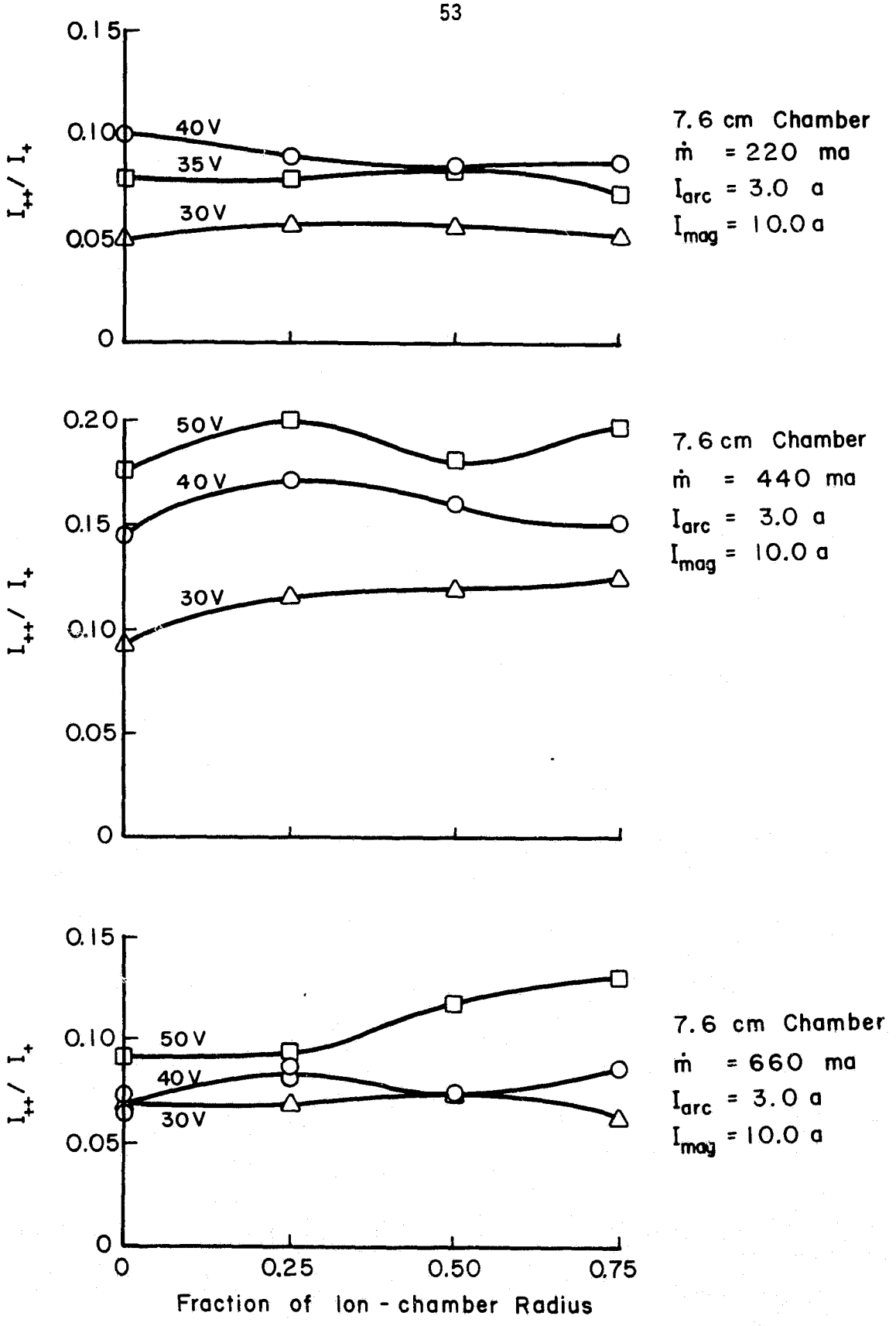

Figure 30. Fraction of doubly ionized xenon for various operating conditions.

The variation with propellant flow rate is less clear. Using the same discharge voltage, the double ionization is a maximum for the intermediate flow rate. This apparent discrepancy cannot be resolved with the limited amount of double ionization data available.

The double ionization data for both argon and xenon were insufficient for the integrated correction method of Vahrenkamp[11] to be used. The Langmuir probe data, ion beam profiles, and available double ionization data all indicated fairly uniform plasma conditions in the ion chamber. The simple average of measurements at different radii were therefore used to correct the performance data of this investigation.

In the case of argon, the measured beam current is

$$I_B = I_+ + I_{++}$$

and the measured utilization is

$$\eta_{u,meas} = (I_+ + I_{++})/I_o,$$

where I_o is the equivalent current for the neutral flow assuming one electronic charge per propellant atom. The actual utilization is

$$\eta_{u,act} = (I_+ + I_{++}/2)/I_o.$$

The correction for utilization is thus

$$\frac{\eta_{u,act}}{\eta_{u,meas}} = \alpha = \frac{I_+ + I_{++}/2}{I_+ + I_{++}}$$

or

$$\alpha = \frac{1 + I_{++}/2I_+}{1 + I_{++}/I_+}$$

Using average ratios of I_{++}/I_+, the correction factor α was 0.97-0.99 for all voltages and argon flows.

For xenon propellant, the presence of aluminum resulted in an additional correction. The measured beam current is

$$I_B = I_+ + I_{++} + I_{+,Al}$$

and the measured utilization is

$$\eta_{u,meas} = (I_+ + I_{++} + I_{+,Al})/I_o$$

The actual utilization, though, is the same as given for argon. This gives a correction factor of

$$\frac{\eta_{u,act}}{\eta_{u,meas}} = \beta = \frac{I_+ + I_{++}/2}{I_+ + I_{++} + I_{+,Al}}$$

or

$$\beta = \frac{1 + I_{++}/2I_+}{1 + I_{++}/I_+ + I_{+,Al}/I_+}$$

Using the average ratios of I_{++}/I_+ and $I_{+,Al}/I_+$, the xenon correction factor β was 0.91-0.94 for the 220 and 660 ma equivalent flows. For the 440 ma equivalent flow, this factor was 0.87-0.91.

All data presented in this paper were corrected for double ionization using the correction factors described above. The accuracy of these correction factors is limited by the small amount of double ionization data avilable. The corrections were large enough (particularly for xenon) that corrections of limited accuracy were felt preferable to no corrections.

PERFORMANCE CORRELATION

A wider range of chamber length was included in this investigation than any recent study of discharge-chamber performance. The possibility of correlating performance for different chamber lengths was therefore examined.

The value of the neutral-loss parameter, $N_o m_i \sigma(V_p/A_p)/A_o$, in correlating "knee" performance[12] made it a promising candidate for a more general performance correlation. In the terminology of this report, N_o equals $I_b(1-\eta_u)/\eta_u$ or $I_o(1-\eta_u)$. Using the last form, the neutral-loss parameter becomes $I_o(1-\eta_u)m_i\sigma(V_p/A_p)/A_o$. Inasmuch as the accelerator system was constant for all data, the effective open area A_o was omitted. Also, use of data for only one gas at a time permitted ion mass m_i and ionization cross section σ to both be omitted. These omissions left $I_o(1-\eta_u)(V_p/A_p)$, where I_o is the total neutral flow rate in amperes and V_p/A_p is the ratio of volume to outside area for the primary electron region. In a multipole thruster, the primary electron region can be taken as the cylindrical volume enclosed by the accelerator system and the inside edges of the pole pieces and anodes. The ratio V_p/A_p is given in meters.

For a discharge-loss parameter, some means of compensating for changes in wall area (and associated wall losses) was required. The simplest approach was to multiply experimental discharge losses (ev/ion) by the ratio of beam area to primary electron region area, A_b/A_p. The distribution of actual losses is more complicated, but the use of this simple area ratio might be expected to give a first-order correction.

The ion chamber data for 1000 ma equivalent with four chamber lengths are plotted in Figure 31 in terms of the neutral-loss and discharge-loss parameters. It is evident that these parameters give a high degree of data correlation.

When a range of argon flow rates was included with the range of chamber lengths, Figure 32 was obtained. Although data for each flow rate (with a range of chamber lengths) tended to group together, the data for different flow rates occupied different regions of the plot. The apparent reason for this noncorrelation of different flow rates is illustrated by Figure 33. The data for a single ion chamber operated at different propellant flows tend to come togetner at low utilizations and diverge at higher utilizations. If the low utilization portions of the curves have very little slope, the resultant curves appear as in Figure 33(a). If similar points for different flow rates (such as A, B, and C) are to fall on a single point in a generalized plot then it is sufficient to adjust for the different utilizations obtained with different flow rates. If however, the low utilization portions have a substantial slope, then the curves appear as shown in Figure 33(b). The generalization of similar points with different flow rates will then require an adjustment of both discharge loss and propellant utilization. In particular, a variation with propellant flow is not included in the discharge-loss parameter of Figure 31. Dividing the discharge-loss parameter of Figure 31 by the square-root of propellant flow rate was found to give approximately the desired effect. Using this modified parameter, the data of Figure 32 were replotted in Figure 34.

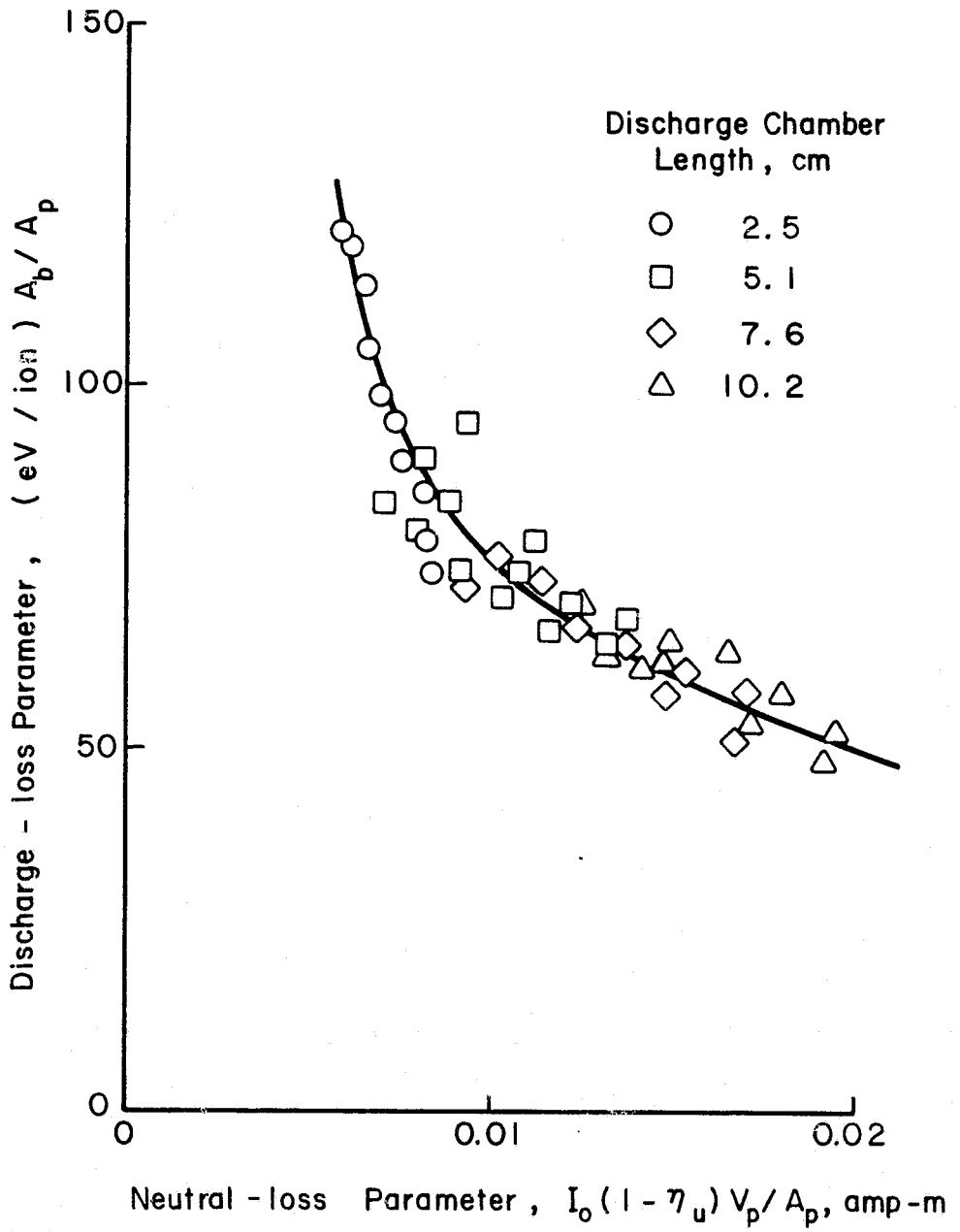

Figure 31. Performance correlation for all discharge chamber lengths at an argon propellant flow rate of 1.00 amperes equivalent.

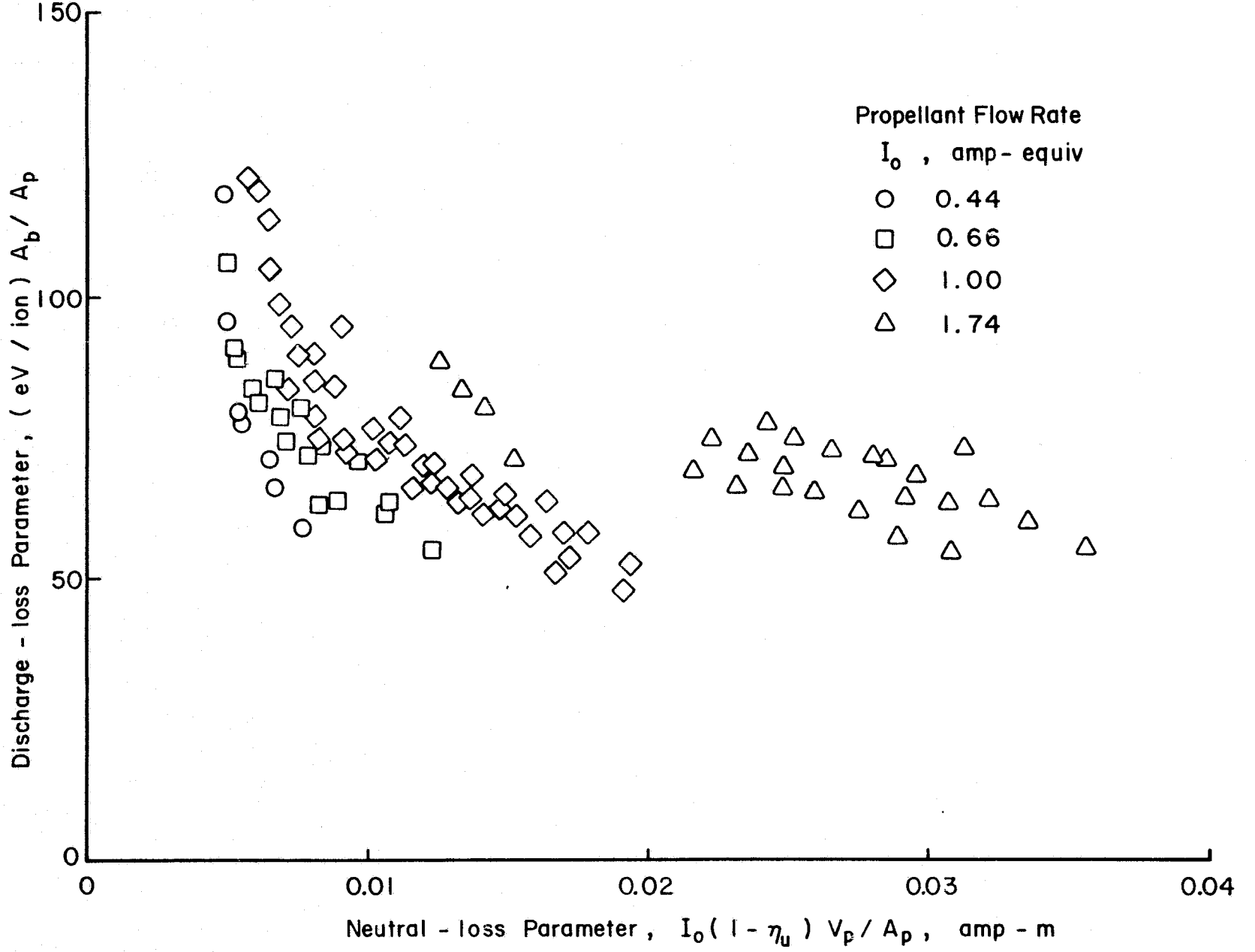

Figure 32. Effect of including all argon propellant flow rates in the correlation of Figure 31.

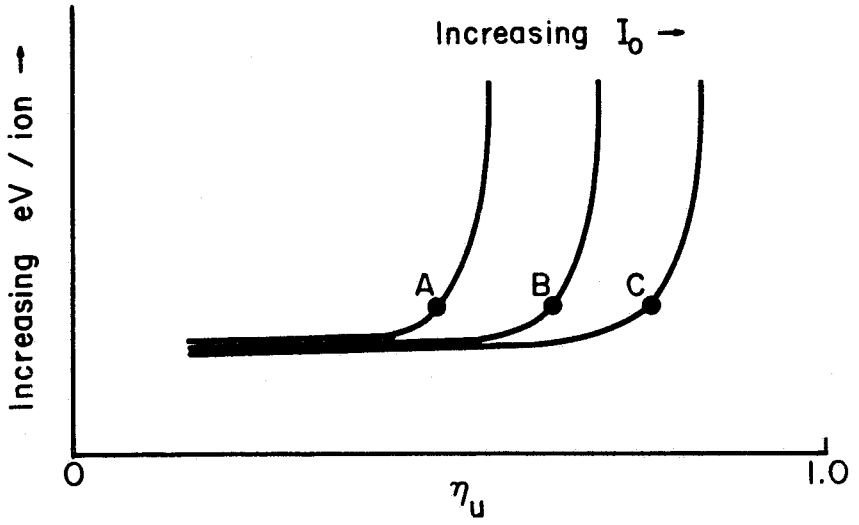

(a) Small Slope at Low Utilization

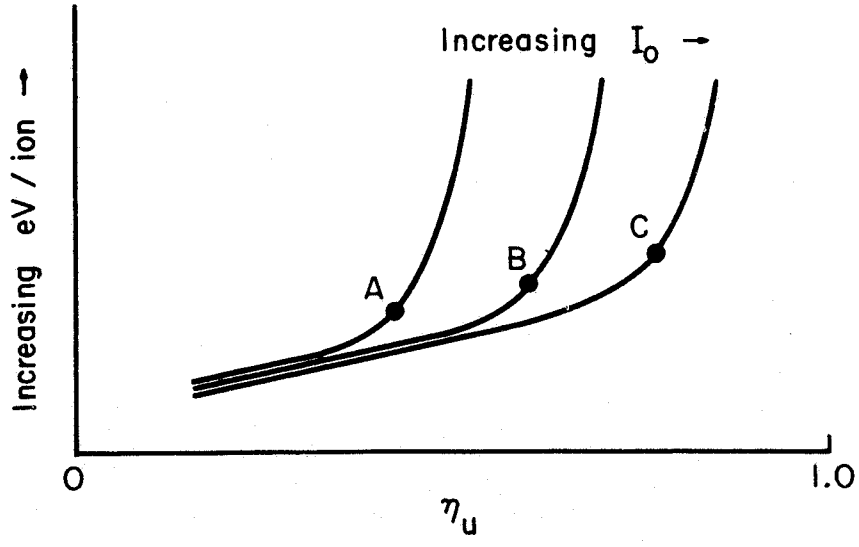

(b) Substantial Slope at Low Utilization

Figure 33. Different types of discharge-loss curves for a single ion-chamber configuration.

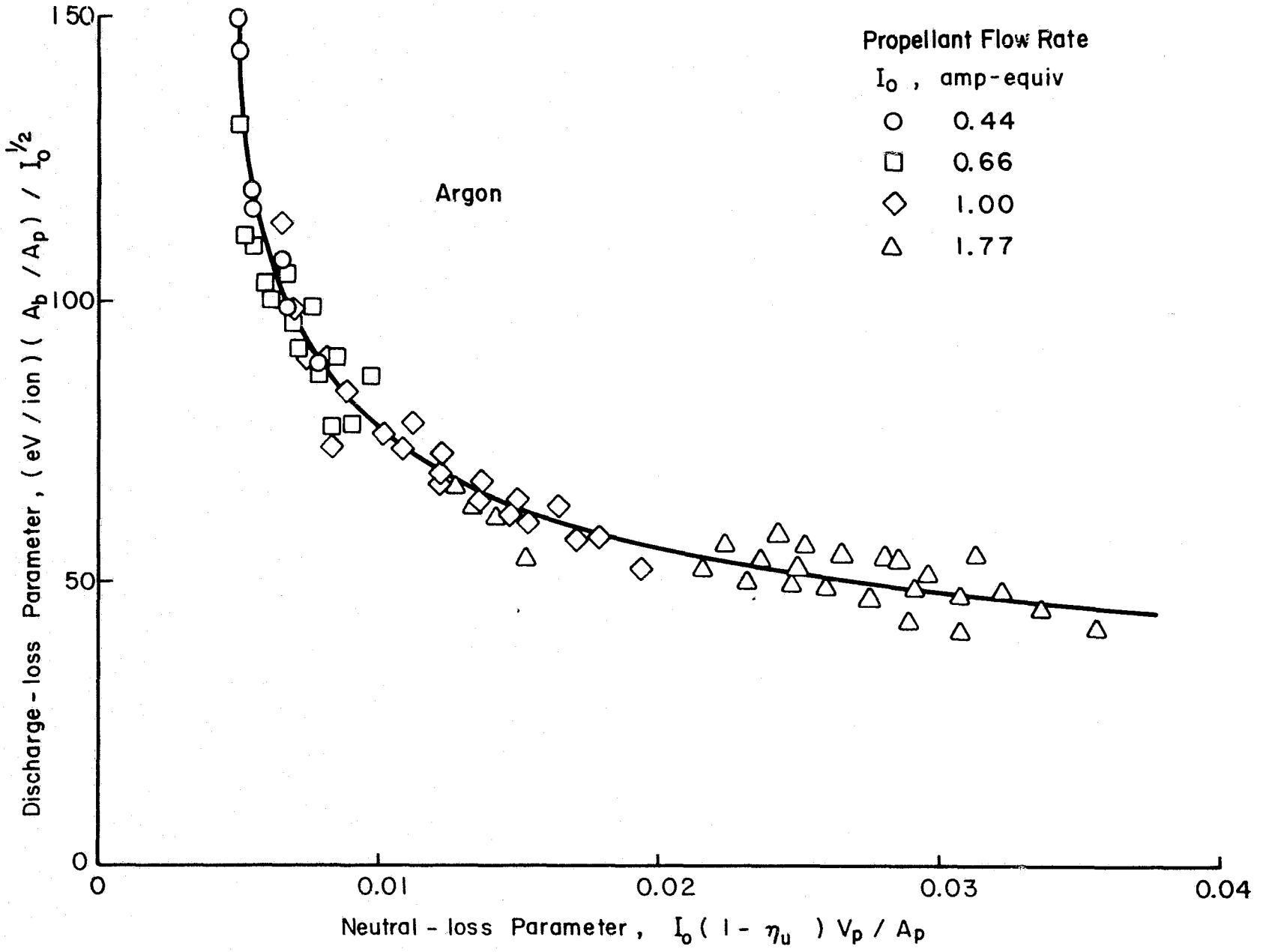

Figure 34. Performance correlation for all discharge chamber lengths and all flow rates for argon propellant.

The data correlation of four chamber lengths and four propellant flow rates is quite good in Figure 34. It should be kept in mind that use of propellant flow rate in the discharge-loss parameter is dependent on the particular shape obtained for the discharge-loss curve. From the discharge-loss curve shapes of Kaufman[13], one might expect curves of the shape of Figure 33(b) and the multipole thruster used herein to be associated with a weak or otherwise inadequate magnetic field. The correction of the lossy corner design (described in the Magnetic Field section) might therefore result in curve shapes similar to those in Figure 33(a). If this is found to be true, the use of propellant flow rate in the discharge-loss parameter may not then be necessary for a good correlation of different flow rates.

The expected neutral loss for the discharge-loss knee was calculated using the method of Kaufman and Cohen[12]. The result corresponded to a neutral-loss parameter of 0.0078 in Figures 31 and 34. This value is in reasonable agreement with the curve shape shown.

A similar analysis was made of xenon data. The equivalent of Figure 34 is shown in Figure 35. The data scatter in Figure 35, though is considerably larger than for Figure 34. The large double-ionization corrections, made on the basis of limited experimental data, are suspected as the cause of this scatter.

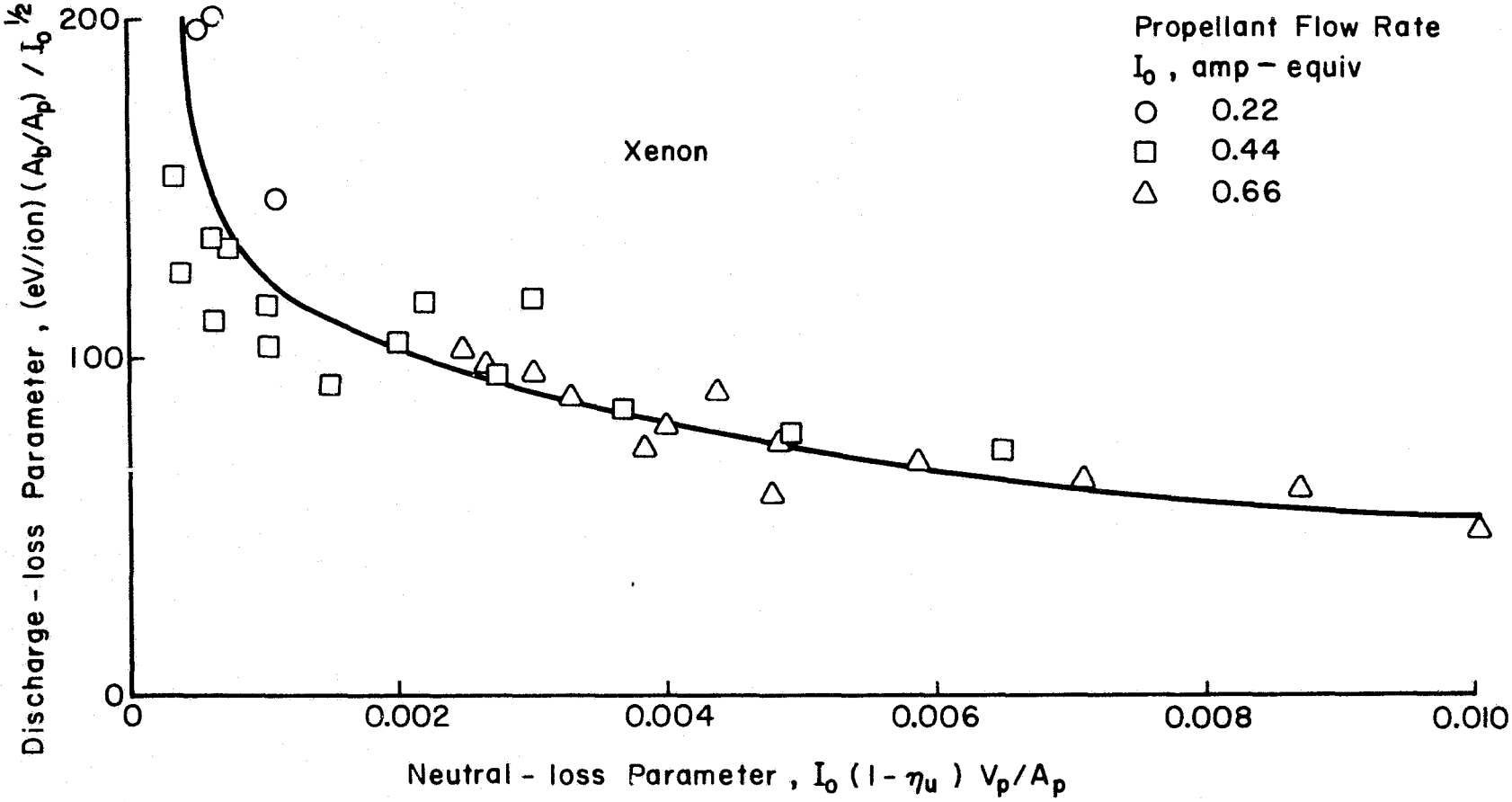

Figure 35. Performance correlation for all discharge chamber lengths and all flow rates for xenon propellant.

POLE-PIECE SIMULATION

A simulated pole-piece configuration was constructed to give additional data on the magnetic-field fringing above an anode. Strips of soft iron were used - 1.5 mm thick, 2.5 cm wide and 15 cm long. A pair of solenoids, each 2.5 cm long, were used to separate each pair of pole pieces and provide a maximum magnetic field equal to that used in the thruster. A pole piece consisted of a pair of soft-iron strips, except for the end pole pieces that used single strips.

The first configuration tested was a single-break corner, as indicated in Figure 36(a). The long dimension of the strips is normal to the paper in this sketch. The fringe field was numerically integrated from a point midway between pole pieces and flush with the inside edges to a point far enough away to have negligible field strength. Away from any corner effects, the typical value of this integral is about 0.35 B_{max} g, where B_{max} is the maximum value on the plane midway between pole pieces and g is the gap between adjacent pole pieces. For comparison, the theoretical value for a single pair of isolated pole pieces is about 0.5. The ratio of the fringe-field integral at the corner (location C) to the integral at the side (location S) is given in Figure 36(a). (The field at location S was found to vary little from one further away, hence was used as representative of any side location. For a 90 degree angle, the ratio of integrals is about 0.65-0.7.)

The smaller fringe field of a corner pole is the same phenomena that was discussed in the Magnetic Field section. One way of compensating for this effect is to increase the general level of magnetic field at the corner location. From Figure 36(a), this approach would require

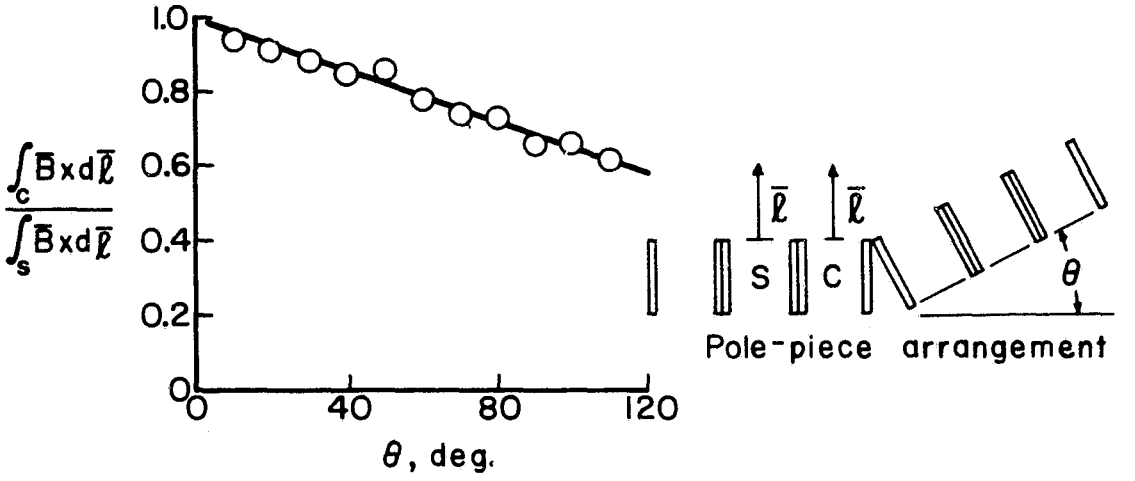

(a) Corner-to-side Ratio of Fringe-field Integrals

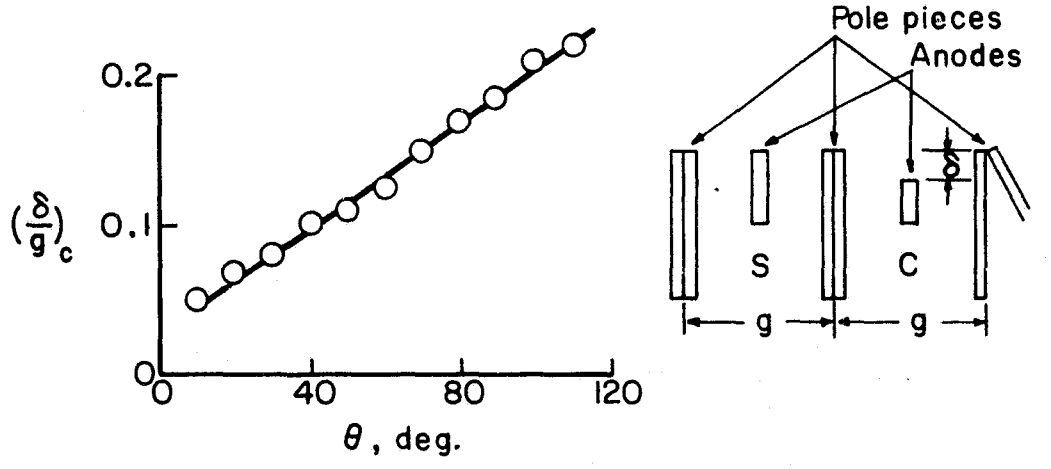

(b) Anode Depression for Equal Fringe-field Integrals

Figure 36. Single-break corner effects for multipole field.

about a 50 percent increase for a 90 degree angle. Another approach would be to recess a corner anode (behind the edges of the pole pieces) to provide the additional field. The numerical integration was carried out between the pole pieces until the field integral at the corner equalled that at the side with this location indicating the amount of recess required for the corner anode. The anode recess is given in Figure 36(b) as a fraction of pole-piece gap. For a 90 degree corner, the corner anode should be recessed about 20 percent of the spacing between pole pieces.

A similar study was made of a double break, the results of which are shown in Figure 37. Two corner locations, C_1 and C_2 are given for the double break (see Figure 37(a)), with different results observed for the two locations. The C_1 location was similar to the C location in the single break, as shown by a similar decrease in fringe integral with increasing angle. The C_2 location (between two C_1 locations), though, showed an increase in fringe integral over much of the angle range investigated.

The anode recess required for a fringe integral equal to that of a side location was also investigated for a double-break corner. As shown in Figure 37(b), the anode recess for a 90 degree corner was found to be about 10 percent of the pole piece gap for the C_1 location. The C_2 location gave an anode position above the pole pieces for most of the angle range covered, and near zero for a 90 degree corner.

The above discussion of Figures 36 and 37 assumes that most anodes will be flush with the inside edges of the pole pieces. Other positions may be found desirable for minimum discharge losses, in which case

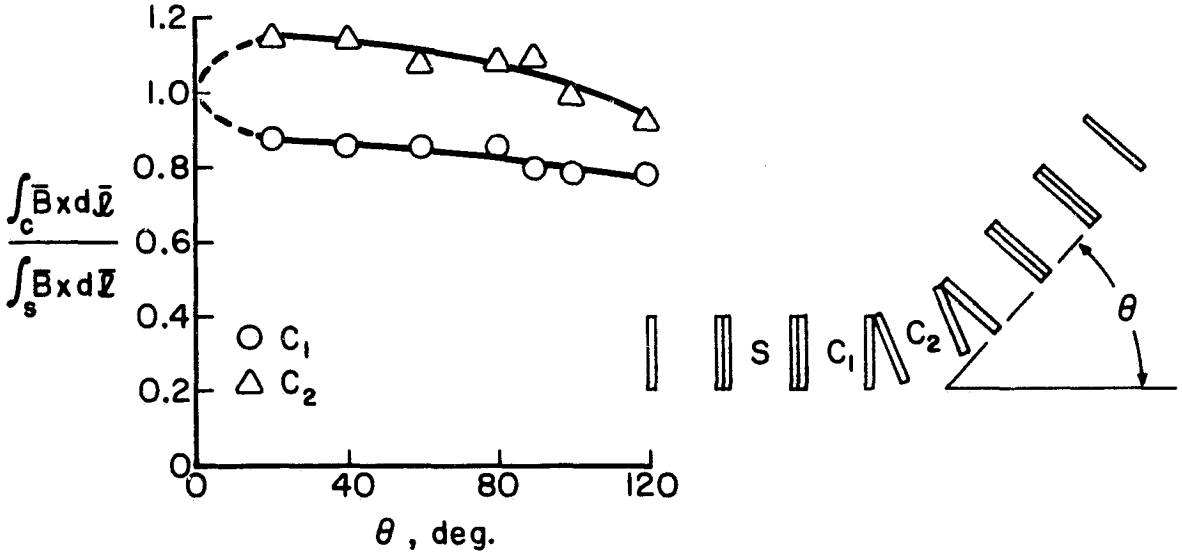

(a) Corner-to-side Ratio of Fringe-field Integrals

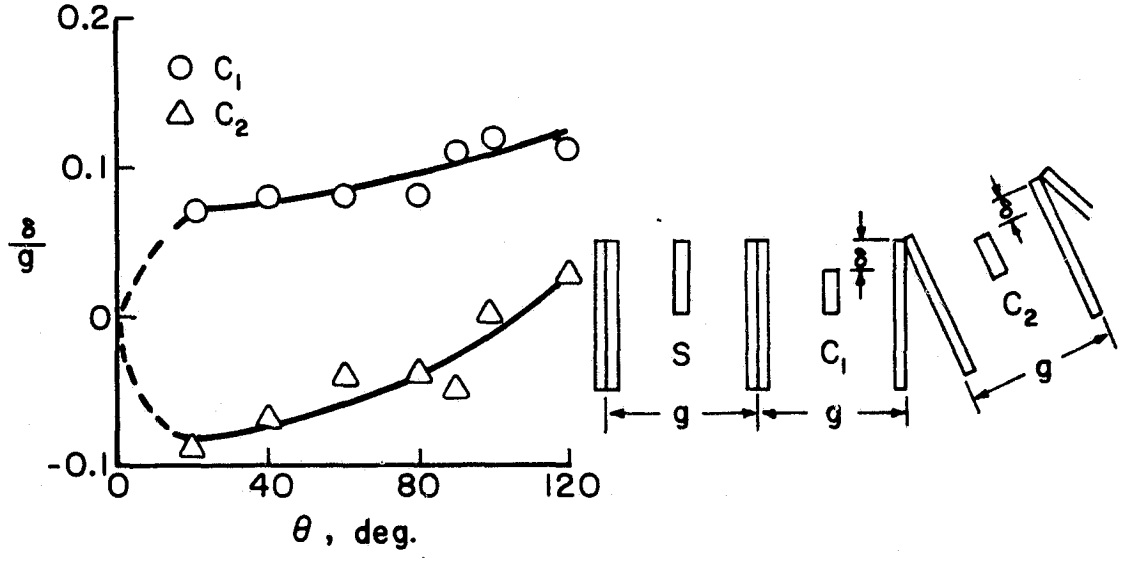

(b) Anode Depression for Equal Fringe-field Integrals

Figure 37. Double-break corner effects for multipole field.

the corner anodes will need a similar repositioning. For example, if most anodes are to be recessed 10 percent of the pole-piece gap, then the corner anodes should be recessed slightly less than 30 percent. Because the incremental field is stronger for a deeper recess, the additional recess should be slightly less than the previously noted 20 percent.

The experimental maximum field was also compared to the theoretical value to provide design information similar to that in Figure 10. At a maximum magnetic induction of 1.2 Tesla (in the soft-iron solenoid cores), the field in the air gap was 0.7-0.75 of the theoretical value in which the air gap is considered the only magnetic reluctance. This result is in reasonable agreement with the 8 magnet configuration of Figure 10, in which the high magnetic induction was also concentrated in a small part of the magnetic circuit.

CONCLUDING REMARKS

The multipole thruster of the type investigated herein has been shown capable of low discharge losses and flat ion-beam profiles with a minimum of optimization. Minimum discharge losses were in the 200-250 ev/ion range for both argon and xenon. Flatness parameters were typically in the 0.70-0.75 range, which approaches the best values obtained previously in highly optimized designs.

The design used employs low magnetic field strengths compared to other multipole designs. Because of this low field strength and the extensive use of flat or cylindrical sheet-metal parts, the design employed is suited to rapid optimization and scaling. When this approach is properly exploited, it should be possible to rapidly translate initial performance specifications into easily fabricated, high performance prototypes.

The knowledge required for proper exploitation of this multipole design is considerable, but substantial progress has already been made in a number of areas. As examples:

1. The magnitude required for the magnetic field and the associated scaling laws have both been determined.

2. The ion-chamber corner losses have been evaluated and corrective techniques been proposed.

3. The experimental neutral loss rates are in reasonable agreement with predicted values.

4. The performance has been correlated for a wide range of ion-chamber lengths and operating conditions. Similar correlations for improved versions of the multipole design should facilitate design for new applications.

REFERENCES

1. Reader, P. D., "The Operation of an Electron-Bombardment Ion Source with Various Gases," NASA TM X-52006 (1964).

2. Schertler, R. J., "Preliminary Results of the Operation of a SERT II Thruster on Argon," AIAA Paper No. 71-157 (1971).

3. Byers, D. C. and P. D. Reader, "Operation of an Electron-Bombardment Ion Source using Various Gases," NASA TN D-6620 (1971).

4. Martin, A. R., "Design and Operation of an Ion Engine using the Rare Gases," Journal of the British Interplanetary Society, Vol. 26, pp. 742-752 (1973).

5. Martin, A. R., "Physical Behavior of some Biowaste Gases in an Ion Engine," AIAA Paper No. 73-1113 (1973).

6. Moore, R. D., "Magneto-Electrostatically Contained Plasma Ion Thruster," AIAA Paper No. 69-620 (1969).

7. Ramsey, W. D., "12-cm Magneto-Electrostatic Containment Mercury Ion Thruster Development," J. Spacecraft and Rockets, Vol. 9, pp. 318-321 (1972).

8. Beattie, J. R., in "15 cm Diameter Ion Thruster Research" (by P. J. Wilbur) pp. 14-44, NASA Contract Report CR-134755 (1974).

9. Wilbur, P. J., "Experimental Investigation of a Throttlable 15 cm Hollow Cathode Ion Thruster," NASA Contract Report CR-121038 (1972).

10. Beattie, J. R., in "15 cm Diameter Ion Thruster Research" (by P. J. Wilbur) pp. 73-80, NASA Contract Report CR-134755 (1974).

11. Vahrenkamp, R. P., "Measurement of Double Charged Ions in the Beam of a 30 cm Mercury Bombardment Thruster," AIAA Paper No. 73-1057 (1973).

12. Kaufman, H. R., and Cohen, A. J., "Maximum Propellant Utilization in an Electron-Bombardment Thruster," in Proc. Symp. Ion Sources and Formation Ion Beams, pp. 61-68, Brookhaven Nat. Lab. (1971).

13. Kaufman, H. R., "Ion-Thruster Propellant Utilization," NASA TN-D6591 (1971).

APPENDIX - SYMBOLS

A_b	Beam area (0.0177 m^2 for 15-cm beam), m^2
A_p	Area of primary electron region, m^2
B	Magnetic induction, Tesla
B_{act}	Maximum magnetic induction in magnetic circuit, from measured total flux, Tesla
B_{id}	Maximum magnetic induction in magnetic circuit, calculated with air gap as only reluctance in magnetic circuit, Tesla
g	Gap between adjacent pole pieces, m
I_{arc}	Discharge current, amp
I_b	Beam current, amp
I_{mag}	Magnet current, amp
I_o	Propellant flow rate, amp-equivalent
I_+	Current of singly ionized atoms, amp
I_{++}	Current of doubly ionized atoms, amp
ℓ	Distance from anode, m
$\dot{m}$	Propellant flow rate, amp-equivalent
r_c	Cyclotron radius of electron, m
V_{arc}	Discharge potential difference, volts
V_p	Volume of primary electron region, m^3
α, β	Correction factors for propellant utilization
δ	Depression of anode relative to adjacent pole pieces, m
η_u	Propellant utilization